Thermal transitions, pseudogap behavior, and BCS-BEC crossover in Fermi-Fermi mixtures

Madhuparna Karmakar
Harish Chandra Research Institute, Chhatnag Road, Jhunsi, Allahabad-211019, India;
Homi Bhabha National Institute, Training School Complex, Anushakti Nagar, Mumbai 400085, India;
and Department of Physics, Indian Institute of Technology Madras, Chennai-600036, India

(Received 27 July 2017; published 23 March 2018)

We study the mass imbalanced Fermi-Fermi mixture within the framework of a two-dimensional lattice fermion model. Based on the thermodynamic and species-dependent quasiparticle behavior, we map out the finite-temperature phase diagram of this system and show that unlike the balanced Fermi superfluid, there are now two different pseudogap regimes as PG-I and PG-II. While within the PG-I regime both the fermionic species are pseudogapped, PG-II corresponds to the regime where pseudogap feature survives only in the light species. We believe that the single-particle spectral features that we discuss in this paper are observable through the species-resolved radio-frequency spectroscopy and momentum-resolved photoemission spectroscopy measurements on systems such as 6_{Li}-40_{K} mixture. We further investigate the interplay between the population and mass imbalances and report that at a fixed population imbalance, the BCS-BEC crossover in a Fermi-Fermi mixture would require a critical interaction (U_c) for the realization of the uniform superfluid state. The effect of imbalance in mass on the exotic Fulde-Ferrell-Larkin-Ovchinnikov superfluid phase has been probed in detail in terms of the thermodynamic and quasiparticle behavior of this phase. It has been observed that in spite of the s-wave symmetry of the pairing field, a nodal superfluid gap is realized in the Larkin-Ovchinnikov regime. Our results on the various thermal scales and regimes are expected to serve as benchmarks for the experimental observations on 6_{Li}-40_{K} mixture.

DOI: 10.1103/PhysRevA.97.033617

I. INTRODUCTION

Ultracold atomic gases with the tunability of their interaction strength have proved to be a suitable quantum simulator for several many-body phenomena, a principal one being the realization of exotic superfluid phases in Fermi gases [1–4]. The experimental realization of the same continues to be illusive so far but that has not prevented the theoretical investigation of the various possibilities, viz., p-wave superfluid [5–13], imbalanced superfluid [14–17], superfluid with hetero-Cooper pairs [18–38], and Fermi superfluid with spin-orbit interaction [39–42].

Among the various possibilities, imbalanced Fermi superfluids is one which has been widely explored. Imbalance in Fermi superfluids can be realized through (i) population imbalance or (ii) mass imbalance. While the former has been investigated in detail both experimentally [43–47] and theoretically [48–54], studies carried out on unequal mass Fermi-Fermi mixtures are relatively few [32,35,38,55–59]. Experimentally, a mass imbalanced Fermi-Fermi mixture is achievable in a 6_{Li}-40_{K} mixture. While superfluidity in such a system is yet to be attained in experiments, the Fermi degenerate regime [19,22] as well as the Feshbach resonance between 6_{Li} and 40_{K} atoms [18,21,22] and formation of 6_{Li}-40_{K} heteromolecules [20] are already a reality. Furthermore, experimental realization of mixtures of other fermion species (such as 161_{Dy}, 163_{Dy}, 167_{Er}) are expected in future [60,61].

An experimentally addressable aspect of the mass imbalanced mixture is its finite-temperature behavior. It has been reported that for a double-degenerate 6_{Li}-40_{K} mixture the Fermi temperatures are $\mathrm{T}_F^{\mathrm{Li}} = 390$ nK and $\mathrm{T}_F^{\mathrm{K}} = 135$ nK, for Li and K species, respectively [23]. In comparison, for a balanced Fermi gas of 6_{Li}, the Fermi temperature is known to be $T_F = 1.0\ \mu$K [62] with the corresponding T_c scale being $T_c \sim 0.15 T_F$ [63]. While it is evident that in case of the mass imbalanced Fermi-Fermi mixture the thermal scales are significantly suppressed, the qualitative and quantitative behaviors of the same are hitherto unknown.

Keeping in pace with the experiments, efforts have been put in to theoretically investigate the behavior of mass imbalanced Fermi-Fermi mixtures within the framework of continuum models. Density functional theory combined with local density approximation [56], functional renormalization group studies, etc., have been carried out on mass imbalanced Fermi mixture at unitarity [55]. The study involved inclusion of fluctuations beyond the mean field and predicted the possibility of inhomogeneous superfluid state. The problem has also been investigated using mean field theory (MFT), taking into account the effects of Gaussian fluctuations [35,64]. The authors mapped out the polarization-temperature phase diagram at different mass as well as population imbalances at and away from unitarity. It was shown that while for a mass balanced system, instability towards a supersolid phase accompanied by a Lifshitz point is observed only at weak interactions, the imbalance in mass promotes this behavior and makes it observable even at unitarity. Among the other techniques, T-matrix and extended T-matrix approaches [38,57,58] are utilized to determine the thermal scales of the mass imbalanced mixture, both in terms of its thermodynamic as well as quasiparticle behavior. It was observed that unlike the balanced Fermi gas, the Fermi-Fermi mixture with imbalance in mass consists of more than one pseudogap scale [38,57].

Interestingly, within the framework of a lattice fermion model, most of the theoretical investigations on imbalanced Fermi gases are carried out on systems with imbalance in population, through improvised numerical and analytic techniques [48–52,65–67]. For the mass imbalanced mixture there are only few attempts that have been made within the framework of lattice fermion model. For example, the ground-state behavior of one-dimensional mass imbalanced system has been studied through quantum Monte Carlo (QMC) calculations [59]. Recently, a nonperturbative lattice Monte Carlo calculation was carried out to address the ground state of Fermi-Fermi mixture in two dimensions (2D) [68]. The study revealed that a mean field approach to the problem grossly overestimates the ground-state energy of the system. The effect is likely to be more severe at finite temperature where crucial amplitude and phase fluctuations are neglected within a mean field scheme.

An estimate of the inadequacy of mean field approach to the problem at finite temperature can be made from the fact that mean field theory overestimates the T_c scales by a factor of more than 4 both in case of balanced [69–74] as well as population imbalanced Fermi superfluids [51]. This is a crucial observation owing to the fact that many of the predictions for imbalanced Fermi superfluids are being made based on the mean field theory.

While there is now a consensus about the thermal behavior of balanced Fermi superfluid [75,76], the same cannot be said about the Fermi-Fermi mixture. Within the purview of lattice fermions, there is certainly a void in our present understanding of such mixtures, especially at finite temperatures. On the other hand, a lattice fermion model is a suitable choice keeping in view the optical lattice experiments that are carried out on ultracold Fermi gases. What is the T_c scale of a mixture such as $6_{\rm Li}$-$40_{\rm K}$? How does such a system behave across the BCS-BEC crossover and, most importantly, how does the pseudogap physics play out in the background of an imbalance of fermionic masses in the system? While an experimental investigation to answer such questions is awaited, one can certainly make theoretical predictions.

Motivated by these questions, in this paper we present a detailed finite-temperature analysis of mass imbalanced Fermi mixture within the framework of lattice fermions. We use a numerical technique which takes into account the phase fluctuations of the ordering field and can access the thermal transitions with quantitative correctness. Apart from investigating the behavior of mass imbalanced system across the BCS-BEC crossover, we also investigate the interplay of mass and population imbalances. Before making quantitative predictions about the $6_{\rm Li}$-$40_{\rm K}$ mixture, we have discussed how the exotic Fulde-Ferrell-Larkin-Ovchinnikov (FFLO) superfluid phase reacts to the imbalance in mass in terms of thermodynamic and quasiparticle behavior. We highlight our principal observations below before proceeding to discuss the numerical technique and the results obtained from the same.

(i) Imbalance in mass leads to strong suppression of T_c across the BCS-BEC crossover regime. Close to unitarity ($U \sim 4t_L$) for a mass balanced $6_{\rm Li}$ gas $T_c^{\rm bal} \sim 0.15t_L$ [51] (where t_L is the kinetic energy of the light fermion species, discussed later) while for the $6_{\rm Li}$-$40_{\rm K}$ mixture $T_c \sim 0.03t_L$.

(ii) For $T > T_c$, two pseudogap regimes are realized as PG-I and PG-II regimes, corresponding to regions where both and only the lighter fermion species are pseudogapped, respectively. Close to unitarity, the heavy species is pseudogapped up to $T \sim 58.5$ nK, while in the light species the pseudogap survives up to $T > 108$ nK.

(iii) In presence of population imbalance, uniform superfluid state (with zero momentum pairing) is realized only beyond a critical interaction U_c. This is in remarkable contrast to the balanced case where any arbitrarily small attractive interaction gives rise to a stable uniform superfluid.

(iv) Imbalance in population leaves its imprint on the superfluid gap. In spite of an isotropic s-wave interaction, finite-momentum scattering gives rise to "nodal" superfluid gap.

The rest of the paper is organized as follows. In Sec. II we discuss about the model and the numerical method that has been used to study the imbalanced Fermi mixture. Section III discusses our results for population balanced and imbalanced systems with imbalance in mass. We further present quantitative estimates of the thermal scales corresponding to the $6_{\rm Li}$-$40_{\rm K}$ mixture. We touch upon certain computational issues in the discussion Sec. IV and conclude with Sec. V.

II. MODEL, METHOD, AND INDICATORS

A. Model

We study the attractive Hubbard model on a square lattice with the fermion species having unequal masses, additionally they are being subjected to an imbalance in population

$$H = H_0 - h\sum_i \sigma_{iz} - |U|\sum_i n_{i\uparrow}n_{i\downarrow}, \qquad (1)$$

where $H_0 = \sum_{i,j,\sigma}(t_{ij\sigma} - \mu\delta_{ij})c^\dagger_{i\sigma}c_{j\sigma}$, with $t_{ij\sigma} = -t_\sigma$ only for nearest-neighbor hopping and is zero otherwise. σ corresponds to the $\uparrow$ and $\downarrow$ spin species of fermions, henceforth referred as L and H, respectively, where H stands for the heavy-fermion species and L for the lighter one. $t_\sigma \propto 1/m_\sigma$ takes into account the unequal masses of the fermion species; t_L serves as the energy scale in the problem in terms of which the various quantities are measured. We define the mass imbalance ratio as $\eta = m_L/m_H$, where m_H and m_L are the effective masses of the two species. $\eta = 1$ thus correspond to the mass balanced situation. We measure the population imbalance in terms of an "effective field" $h = (1/2)(\mu_L - \mu_H)$, where μ_L and μ_H correspond to the chemical potential of the light- and heavy-fermion species, respectively. The polarization is defined as $m = \langle n^i_L - n^i_H\rangle$, with n^i's being the corresponding number density of the fermion species.

For the system under consideration, we want to explore the physics beyond the weak coupling, which requires one to retain the fluctuations beyond the mean field theory. For this we use a single-channel Hubbard-Stratonovich decomposition of the interaction in terms of an auxiliary complex scalar field $\Delta_i(\tau) = |\Delta_i(\tau)|e^{i\theta_i(\tau)}$. A complete treatment of the problem requires retaining the full (i,τ) dependence of the Δ, a target that can be achieved only through imaginary-time QMC. The present technique known as the static auxiliary field (SAF) Monte Carlo [77,78] ignores the temporal fluctuations but retains the complete spatial fluctuations of Δ_i. This approximation makes the technique akin to the mean field theory at $T = 0$, but retains the amplitude and phase fluctuations of Δ_i at finite temperatures, which controls the thermal scales. In the language of Matsubara frequency, SAF retains fluctuations corresponding to $\Omega = 0$ mode only. A detailed account of our technique can be found in Ref. [51].

The effective Hamiltonian is

$$H_{\text{eff}} = H_0 - h \sum_i \sigma_{iz} + \sum_i (\Delta_i c_{i\uparrow}^\dagger c_{i\downarrow}^\dagger + \text{H.c.}) + H_{cl}, \quad (2)$$

where $H_{cl} = \sum_i \frac{|\Delta_i|^2}{U}$ is the stiffness cost associated with the now "classical" auxiliary field. The pairing field configurations in turn are controlled by the Boltzmann weight

$$P\{\Delta_i\} \propto \text{Tr}_{c,c^\dagger} e^{-\beta H_{\text{eff}}}. \quad (3)$$

This is related to the free energy of the fermions in the configuration $\{\Delta_i\}$. For large and random $\{\Delta_i\}$, the trace has to be computed numerically. For this we generate equilibrium $\{\Delta_i\}$ configurations by Monte Carlo technique, diagonalizing the fermion Hamiltonian H_{eff} for each attempted update.

B. Numerical method

Even though MFT is frequently used to study the imbalance Fermi superfluids, it is essential to retain the crucial thermal fluctuations as one moves beyond the weak coupling regime. The issue has been widely discussed in the context of BCS-BEC crossover in balanced Fermi systems [76,79–90]. For analyzing the ground state and finite-temperature behavior of the mass imbalanced system, we have employed variational minimization and a Monte Carlo simulated annealing, respectively.

1. Simulated annealing by Monte Carlo

The SAF scheme can access significantly larger system sizes ($\sim 40 \times 40$) as compared to what can be accessed through QMC. In order to make the study numerically less expensive, the Monte Carlo is being implemented through a cluster approximation [51,91], wherein instead of diagonalizing the entire lattice of dimension $L \times L$ for each attempted update, we diagonalize a cluster of size $L_c \times L_c$ surrounding the update site. For most of the results presented in this paper we have used a lattice of size $L = 24$, with the cluster size being $L_c = 6$, for typically 4000 Monte Carlo steps.

2. Variational minimization scheme

At zero temperature, the ground state of the system is determined by minimizing the energy over the static configurations of the pairing field Δ_i. The procedure is carried out over the (U, h, η) space, for the pairing field amplitude being defined as $|\Delta_i| \propto \Delta_0 \cos(\mathbf{q}.\mathbf{r_i})$, which takes into account modulations in the pairing field amplitude; here, Δ_0 is assumed to be real and positive. $\mathbf{q}$ is the modulation wave vector and for the balanced (uniform) superfluid phase $\mathbf{q} = 0$. We have also verified the situation with modulations in the pairing field phases but have found it to be energetically unfavorable over the parameter regime under consideration. For the regime of interest $h_{c1} < h < h_{c2}$ (where h_{c1} and h_{c2} are critical population imbalances, discussed later), the modulated superfluid state is of Larkin-Ovchinnikov (LO) type.

C. Parameter regime and indicators

For the results presented in this paper, the interaction ($U = 4t_L$) is set to be close to unitarity, unless specified otherwise. The implementation of a real-space simulation technique leads to restriction on the system sizes that can be accessed. Smaller interactions ($U \leqslant 2t_L$) requires larger system sizes since the $T = 0$ coherence length ξ_0 becomes large. Setting $U = 4t_L$ we have explored the mass imbalance over the regime $\eta \sim [0:1]$ and population imbalance $h/t_L \sim [0:1.50]$. The calculations are carried out at a fixed net chemical potential of $(\frac{1}{2})(\mu_L + \mu_H) = -0.2t_L$. Along the selected cross sections across the parameter space we characterize the phases based on the following thermodynamic and quasiparticle indicators: (i) pairing field structure factor $[S_\Delta(\mathbf{q})]$, (ii) polarization ($m = \langle n_L^i - n_H^i \rangle$), (iii) pair correlation $[\Gamma(\mathbf{q})]$, (iv) momentum-resolved spectral function $A_\sigma(\mathbf{k},\omega)$ (where $\sigma = L, H$), (v) low-energy spectral weight $A(\mathbf{k},0)$ distribution at the Fermi level, (vi) species-resolved occupation number $[n_\sigma(\mathbf{k})]$, and (vii) species-resolved fermionic density of states (DOS) $[N_\sigma(\omega)]$. We define these indicators below:

$$S_\Delta(\mathbf{q}) = \frac{1}{N^2} \sum_{i,j} \langle \Delta_i \Delta_j^* \rangle e^{i\mathbf{q}.(\mathbf{r}_i - \mathbf{r}_j)},$$

$$\Gamma(\mathbf{q}) = \sum_{ij} \Gamma_{ij} e^{i\mathbf{q}.(\mathbf{r}_i - \mathbf{r}_j)}, \quad \text{where } \Gamma_{ij} = \langle c_{iH}^\dagger c_{iL}^\dagger \rangle \langle c_{jL} c_{jH} \rangle,$$

$$A_\sigma(\mathbf{k},\omega) = -(1/\pi)\text{Im}G_\sigma(\mathbf{k},\omega),$$

$$A_\sigma(\mathbf{k},0) = -(1/\pi)\text{Im}G(\mathbf{k},\omega \to 0),$$

$$N_L(\omega) = \left\langle (1/N) \sum_{i,n} |u_n^i|^2 \delta(\omega - E_n) \right\rangle,$$

$$N_H(\omega) = \left\langle (1/N) \sum_{i,n} |v_n^i|^2 \delta(\omega + E_n) \right\rangle.$$

Here, $G_\sigma(\mathbf{k},\omega) = \lim_{\delta \to 0} G_\sigma(\mathbf{k},i\omega_n)|_{i\omega_n \to \omega + i\delta}$ where $G_\sigma(\mathbf{k},i\omega_n)$ is the imaginary frequency transform of $\langle c_{\mathbf{k}\sigma}(\tau) c_{\mathbf{k}\sigma}^\dagger(0) \rangle$. u_n^i and v_n^i are the Bogoliubov–de Gennes (BdG) eigenvectors corresponding to the eigenvalues E_n for the configurations under consideration. $N = L^2$ are the number of lattice sites.

III. RESULTS

In this section, we discuss the results obtained through our numerical simulations. We categorize our observations in two groups, viz., (i) mass imbalanced Fermi-Fermi mixture with balanced population and (ii) mass imbalanced Fermi-Fermi mixture with population imbalance. Within each category, we discuss the ground state and finite-temperature behavior separately.

A. Population balanced Fermi-Fermi mixture

Population balanced Fermi gas corresponds to the situation when the fermionic species are being subjected to equal chemical potential. In the context of ultracold atomic gases, such a system is realized by loading equal population of two fermion species in the optical lattice.

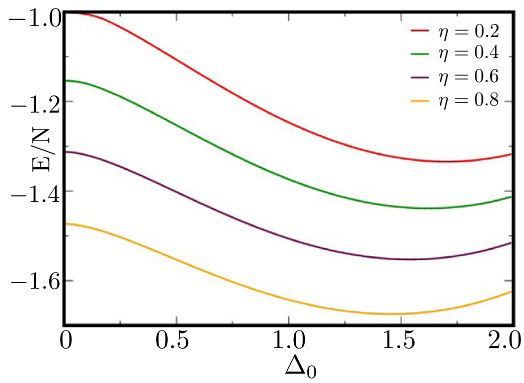

FIG. 1. Variation of free energy density with pairing field amplitude at different mass imbalance ratio and zero population imbalance.

1. Ground state

We begin the discussion of our results in this section with the effect of mass imbalance on the ground state of the system. With h being set to zero, we use the mass imbalance ratio η as the tuning parameter to investigate the various properties. We map out the ground-state phase diagram based on the variational mean field calculation (discussed in the previous section) and in Fig. 1 show the dependence of free energy on the pairing field amplitude Δ_0 and mass imbalance ratio η for the selected interaction strength $U = 4t_L$. The ground-state energy shows a single minima and corresponds to a uniform superfluid state with the pairing field amplitude (Δ_0) being almost independent of the choice of the mass imbalance ratio. Both the pairing field amplitude as well as the superfluid gap at the Fermi level increase monotonically with U. We show these behaviors in the η-U plane in Figs. 2(a) and 2(b), respectively.

The effect of mass imbalance on the quasiparticle dispersion spectra is probed next and we show the corresponding spectral function $A(\mathbf{k},\omega)$ at different mass imbalance ratio in Fig. 3. The $\mathbf{k}$-summed quantity of the spectral function corresponds to the electronic density of states (DOS) and we show the species-resolved variant of the same [$N_\sigma(\omega)$] as the last two panels of Fig. 3. For the computation of both the spectral function and the DOS we have used the Green's function formalism which gives access to large system sizes and thus makes the van Hove singularities prominent. Details of the Green's function formalism are discussed in Sec. IV.

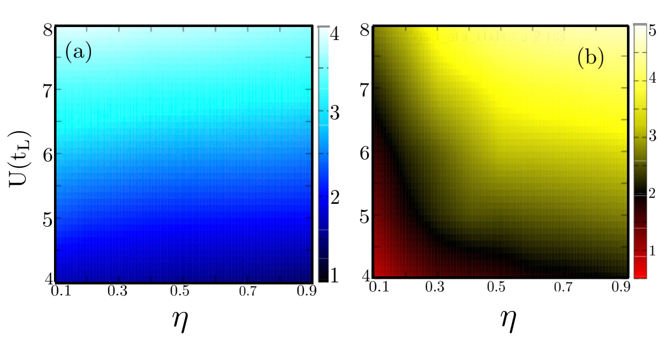

FIG. 2. [$(t_L) \rightarrow$ units of t_L] Ground-state (a) pairing field amplitude and (b) superfluid gap in the η-U plane for the population balanced system. Strong interaction and small mass imbalance ($\eta \rightarrow 1$) leads to a larger pairing field amplitude and gap at the Fermi level.

We observe that at large imbalance in mass there are essentially four branches in the dispersion spectra. Both above and below the Fermi level, the branches intersect each other at $\mathbf{k} = \pi/2$, which gives rise to additional singularities in the form of subgap and supergap states in the DOS. However, there is no spectral weight at the Fermi level which ensures that the underlying ordered state is gapped across the range of η. In a later section, we would find that this behavior is remarkably altered once a population imbalance is introduced in the system. With decreasing mass imbalance, the branches merge together, leading to the well-known two-branched BCS spectra as $\eta \rightarrow 1$ [92].

In agreement with the behavior of the spectral function, we observe that for the system at or close to the mass balanced situation, the species-resolved DOS exhibits prominent hard gap at the Fermi level separated by the characteristic BCS-type coherence peaks. Increasing imbalance gives rise to subgap and supergap states.

2. Finite temperature

Thermal evolution of this system is probed in terms of two thermodynamic quantities, viz., (i) the pairing field structure factor [$S(\mathbf{q})$] and (ii) the pair correlation [$\Gamma(\mathbf{q})$]. While both these quantities essentially give similar information, $\Gamma(q)$ is a more fundamental quantity since it directly probes the fermionic correlations rather than the correlation between the auxiliary fields. Spatial maps of pairing field structure factor as well as pair correlation (not shown here) exhibit a uniform superfluid (BCS-type) low-temperature state with a finite peak at $\mathbf{q} = 0$. Based on these two quantities, we map out the mass imbalance-temperature (η-T) phase diagram at $U = 4t_L$ and show it in Fig. 4(a). Note that in a two-dimensional system such as the present one, thermal transitions are possible only through a Berezinskii-Kosterlitz-Thouless (BKT) transition. The T_c scales discussed here correspond to the BKT transition temperature.

There are two thermal scales in this phase diagram, viz., T_c and T^*, which demarcate the phases as superfluid, pseudogap, and normal. While T_c corresponds to the temperature beyond which the phase coherence in the pairing field is lost, T^* marks the loss of short-range pair correlations leading to the disappearance of superfluidity.

Thermal fluctuations are progressively detrimental with increasing mass imbalance in the system, leading to suppression in T_c as shown in Fig. 4(a). The observation suggests that even though at the ground state there is a large pairing field amplitude, the state is fragile towards thermal fluctuations and rapidly loses phase coherence. The thermal scales T_c and T^* are determined from the pairing field structure factor peaks [$S_\Delta(\mathbf{q})$] shown in Fig. 4(b). Away from the weak coupling regime, the short-range pair correlations survive up to temperatures $T^* \gg T_c$. In the limit of $\eta \rightarrow 1$, we find $T^* \approx 2T_c$. The pseudogap regime is determined based on the temperature dependence of the structure factor and pair correlation peak at $\mathbf{q} = 0$ and T^* corresponds to the temperature at which there is no distinguishable peak in the $S(\mathbf{q})$ and $\Gamma(\mathbf{q})$ at $\mathbf{q} = 0$. Figure 4(a) is one of the important results of this work. It shows how the consideration of phase fluctuations in the numerical framework is important to capture the true thermal scales of

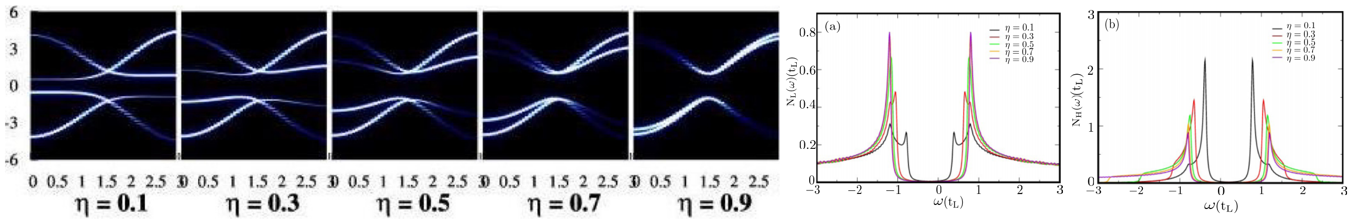

FIG. 3. $[(t_L) \rightarrow$ units of $t_L]$ Ground-state dispersion spectra at different mass imbalance ratio η. The last two panels show the η dependence of the density of states (DOS) for the (a) light- and (b) heavy-fermion species. Note the subgap and supergap features in the DOS at large mass imbalance ratio.

the mass imbalanced superfluid system. A finite-temperature mean field theory (MFT) can track only T^* and thus leads to significant overestimation of T_c. However, even though the thermodynamic measures $S(\mathbf{q})$ and $\Gamma(\mathbf{q})$ are sufficient to quantify the existence of phase coherence in the system, they lack the information about the quasiparticle behavior of the fermionic species. Analyzing the fermionic properties such as single-particle DOS, spectral function, etc. (discussed later), shows us how the information about the quasiparticle behavior significantly alters the phase diagram in Fig. 4(a).

In Fig. 4(c) we show the BCS-BEC crossover at a selected mass imbalance ratio of $\eta = 0.15$, corresponding to the experimentally realized Fermi-Fermi mixture of 6_{Li}-40_{K} [18,19,21,22]. Further, we compare our result with the one obtained for a mass balanced system, so as to demonstrate the suppression of T_c by imbalance in mass.

Across the BCS-BEC crossover, the behavior of the T_c scale is governed by different mechanisms at different coupling regimes. In the weak coupling regime, the thermal scale is determined by the vanishing of the pairing amplitude $(\langle\langle c_{iL}^{\dagger} c_{iH}^{\dagger}\rangle\rangle)$ as $k_B T \sim t e^{-t/U}$. At strong interactions where the system comprises of molecular pairs, the thermal scale is dictated by the phase correlation of the local order parameter and behaves as $k_B T \sim f(n) t^2/U$, where $f(n)$ is a function of number density.

In Fig. 4(d) we show the composite thermodynamic phase diagram in the η-U-T space. A large imbalance in mass suppresses the T_c scale irrespective of the choice of U. For,

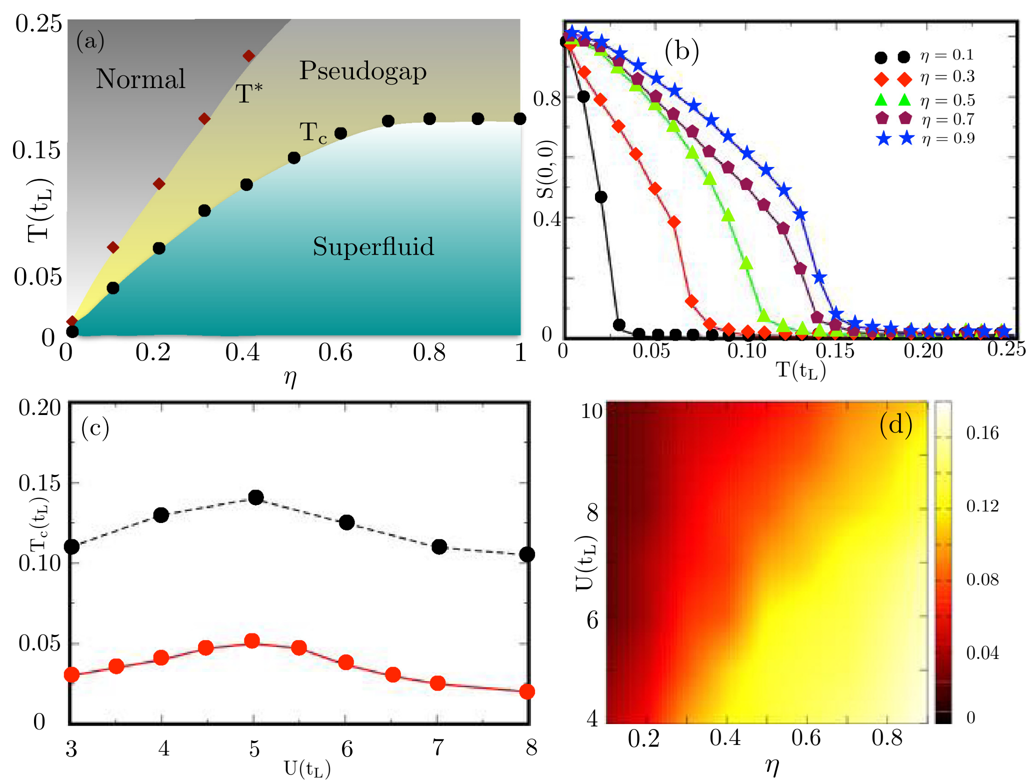

FIG. 4. $[(t_L) \rightarrow$ units of $t_L]$ (a) Effect of mass imbalance (η) on the thermal scales (T_c and T^*) at $U = 4t_L$, for a population balanced system. T_c corresponds to the temperature at which the system loses its phase coherence. Beyond T^* there is no noticeable peak in the pairing field structure factor. (b) Thermal evolution of pairing field structure factor peaks at different mass imbalance ratio. (c) BCS-BEC crossover at $\eta = 0.15$ (red solid line), for a population balanced Fermi-Fermi mixture. Note the suppression in T_c due to mass imbalance, in comparison to the balanced case (black dotted line). (d) BCS-BEC crossover in the η-U plane. The balanced situation corresponds to a large pairing field amplitude and thus a higher T_c.

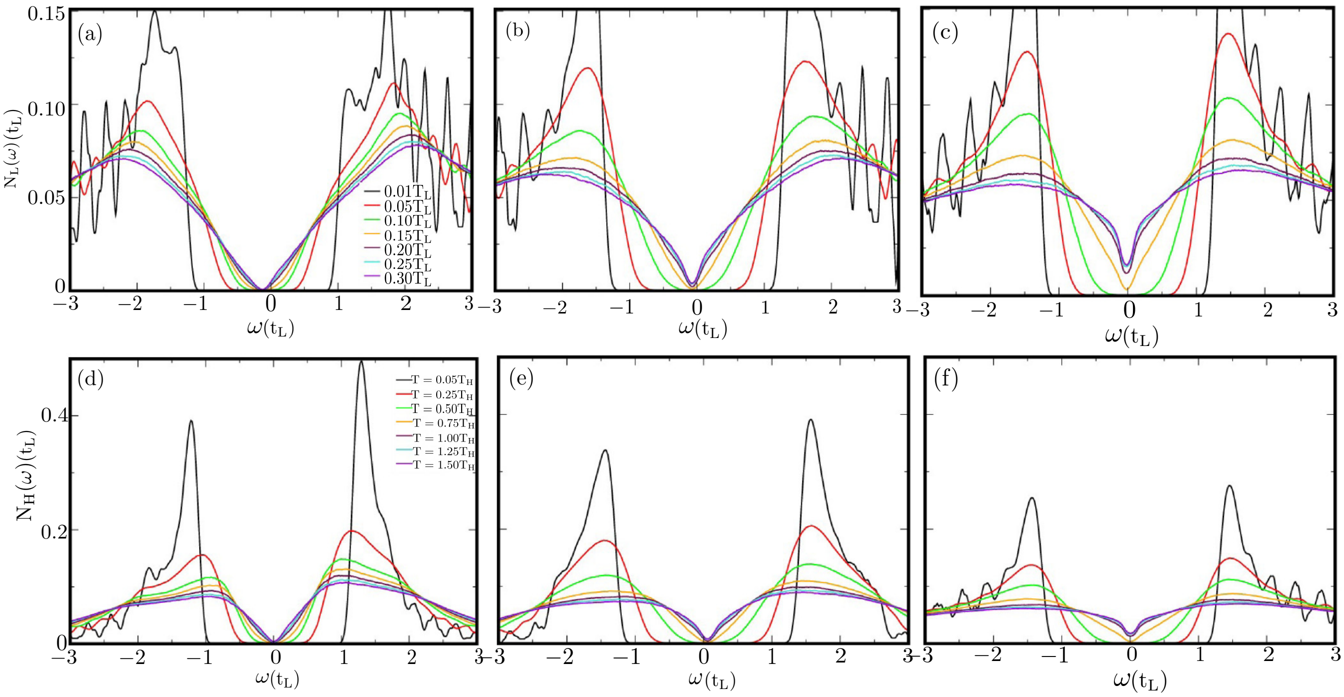

FIG. 5. [$(t_L) \rightarrow$ units of t_L] Thermal evolution of DOS at the Fermi level for the light- [(a)–(c)] and the heavy-fermion [(d)–(f)] species for different mass imbalance ratio of $\eta = 0.2$ [(a) and (d)], $\eta = 0.5$ [(b) and (e)], and $\eta = 0.9$ [(c) and (f)]. At large imbalance in mass the DOS corresponding to the heavy species has coherence peaks with magnitudes significantly larger than its light counterpart. As the system approaches the mass balanced situation the coherence peaks of the heavy species reduce and for $\eta \rightarrow 1$ become equal to that of the light species.

e.g., at $U = 4t_L$, $T_c \sim 0.16t_L$ at $\eta = 0.9$, and progressively reduces to $T_c \sim 0.13t_L$ at $\eta = 0.5$ and to $T_c \sim 0.04t_L$ at $\eta = 0.1$, respectively. The BCS-BEC crossover remains roughly unaffected (except for this suppression) by the change in the mass imbalance ratio, with $U_c \sim 5t_L$ corresponding to unitarity with maximum T_c [76]. We would come back to the concept of unitarity in a lattice fermion model in the discussion section of this paper.

The quasiparticle behavior is discussed next and in Fig. 5 we show the effect of mass imbalance on species-resolved DOS. The effect of mass imbalance on the DOS can be observed through multiple features. A quick look at the magnitude of the coherence peaks of the DOS in Fig. 5 shows that the heavy-fermion species has its coherence peaks significantly larger in magnitude as compared to its lighter counterpart. In Fig. 5 we have shown the species-resolved DOS corresponding to three different mass imbalance ratios as $\eta = 0.2$ [Figs. 5(a) and 5(d)], $\eta = 0.5$ [Figs. 5(b) and 5(e)], and $\eta = 0.9$ [Figs. 5(c) and 5(f)]. While the difference in magnitude of the coherence peaks between the two species is maximum at large mass imbalance, it progressively reduces as the system transits to the balanced situation and at $\eta = 0.9$ they are almost equal, as expected from the mass balanced situation. Second, we observe that the two species are now being subjected to different scaled temperatures and the heavy species experiences a higher temperature as compared to the lighter ones. This is because the kinetic energy contribution of the two species is now different in presence of imbalance in mass. *Thus, there are now two different pseudogap scales in the system* and one needs species-resolved probes such as rf spectroscopy to access them. Finally, at larger imbalance in mass the pseudogap behavior is almost independent of thermal evolution and persists even at high temperatures. It is only close to the mass balanced situation that thermal fluctuations begin to pile up significant weight at the Fermi level. The observation is crucial and suggests that in case of Fermi-Fermi mixtures, thermodynamic quantities such as pairing field structure factor [Fig. 4(a)] significantly underestimate the pseudogap regime. Information about the quasiparticle behavior is essential in this case in order to obtain the complete picture of the thermal behavior of the system. In the later sections, we would observe that inclusion of population imbalance is instrumental in making such mixtures reactive towards temperature and even with large imbalance in mass the pseudogap undergoes significant thermal evolution. This can be summed up as that while an imbalance in mass promotes the pseudogap behavior, an imbalance in population leads to suppression of the pseudogap scales.

A second quasiparticle behavior of interest is the momentum-resolved spectral function $A(\mathbf{k},\omega)$ and we present the species-resolved version of the same for $\mathbf{k} = \{0,0\}$ to $\{\pi,\pi\}$ scan across the Brillouin zone in Fig. 6. While at the low temperature both the species possess prominent spectral gap at the Fermi level, progressive increase in temperature smears out the gap. The thermal disordering temperature corresponding to the two species is now different, leading to two pseudogap scales. Since $t_H < t_L$, the heavy species experiences a higher "scaled" temperature and consequently undergoes faster thermal disordering. It must, however, be noted that even at high temperature there is a very small but noticeable gap at the Fermi level in agreement with the behavior of the DOS. A

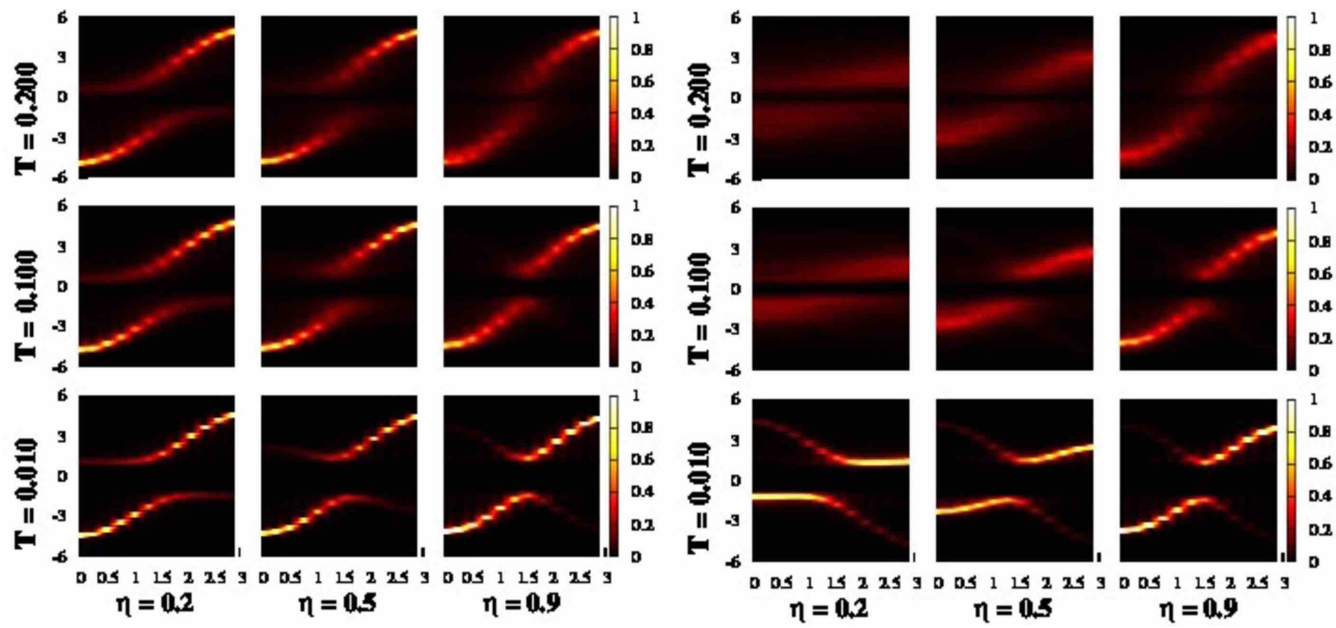

FIG. 6. Thermal evolution of species-resolved [light (left) and heavy (right)] spectral function $A(\mathbf{k},\omega)$ at selected η. All temperatures are measured in terms of t_L, where $t_L = t_H/\eta$. Since the heavy species experiences a higher "scaled" temperature (see text), it undergoes faster thermal disordering.

species-dependent momentum-resolved photoemission spectroscopy measurement is a suitable experimental technique to observe the species-dependent thermal disordering of the spectral functions. While the signature of short-range pair correlation at $T > T_c$ in both the species merely demonstrates the loss of pair coherence, the survival of such short-range pair correlation *only* in the light species would be a true signature of imbalance in mass in the system.

B. Population imbalanced Fermi-Fermi mixture

We now introduce the next level of complexity to the system by adding on an imbalance in population along with the existing mass imbalance. Before proceeding further, we quickly summarize how the imbalance in population is introduced in our model. An imbalance in population can be created through a mismatch in the size of Fermi surface corresponding to the two fermionic species. This in turn can be achieved in two ways, viz., (i) by creating difference in the chemical potential or (ii) by creating difference in the number density of the two fermionic species.

As already mentioned, the imbalance in chemical potential is quantified in terms of an "effective field" h, while a finite polarization m is a measure of imbalance in the number densities. The quantification in terms of finite polarization is more suitable in the context of cold atomic experiments where the population of individual fermionic species to be loaded in the optical lattice can be controlled. For the solid-state systems, the imbalance in population is achieved by applying a Zeeman magnetic field which leads to a chemical potential mismatch. In our work we take this second route and subject the system to an effective Zeeman field ($h \neq 0$), i.e., we control the chemical potential to which the individual species are being subjected, rather than controlling the number density of each species. The presence of population imbalance is expected to suppress the thermal scales at any mass imbalance. In a mass balanced system at a sufficiently large imbalance in the population, a uniform superfluid state can not be realized. It was found that rather than transiting to a polarized Fermi liquid phase the system undergoes transition to a modulated superfluid state with finite momentum ($\mathbf{q} \neq 0$) pairing, known as the Fulde-Ferrell-Larkin-Ovchinnikov (FFLO) state [51,52,93,94]. At weak imbalance in population the system undergoes thermal evolution to a breached pair (BP) state comprising of coexisting superfluidity and finite polarization, a phase which does not have a ground-state counterpart [51]. In the next few sections we discuss the effects of the interplay between population and mass imbalances in the system under consideration.

1. Ground state

As in the population balanced case, we begin the discussion with the ground-state behavior of the system with imbalance in population and mass. The ground-state phase diagram in terms of the effective field h and mass imbalance ratio η is shown in Fig. 7(a). The thermodynamic phases are classified as unpolarized superfluid (USF) (with $\Delta \neq 0$ and $m = 0$), modulated superfluid (LO) (with $\Delta \neq 0$ and $m \neq 0$), and partially polarized Fermi liquid (PPFL) (with $\Delta = 0$ and $m \neq 0$). There are two critical fields in this phase diagram, viz., h_{c1} which correspond to a first-order transition from the USF to the LO state and h_{c2} at which the LO state undergoes a second-order transition to the PPFL phase.

From the perspective of the cold atom experiments, we show the ground-state phase diagram in Fig. 7(b) in the polarization-mass imbalance (m-η) plane. Note that when depicted in terms of polarization, the entire USF regime corresponding to $m = 0$ collapses to the x axis. The first-order transition from USF to

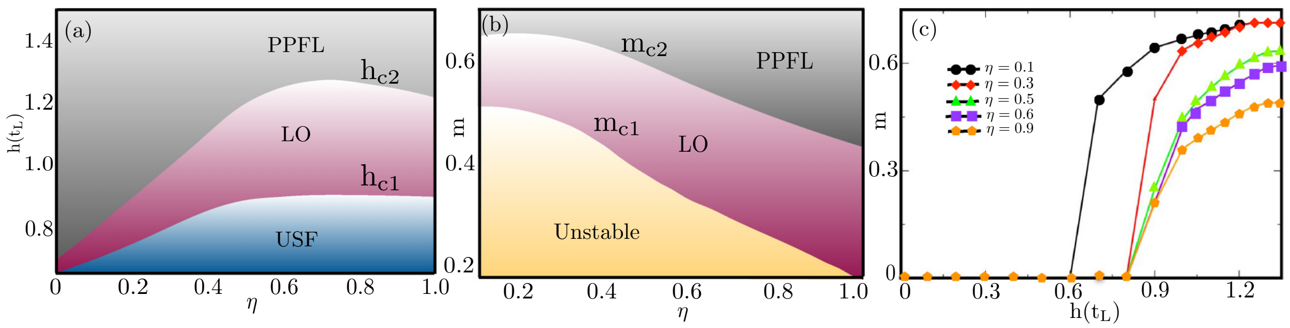

FIG. 7. $[(t_L) \to$ units of $t_L]$ Ground-state phase diagram for the mass imbalanced system as a function of varying population imbalance at $U = 4t_L$, in the (a) η-h and (b) η-m plane. Up to a critical effective field (h_{c1}) say, the system is an unpolarized superfluid (USF). A small η gives rise to a small h_{c1} and beyond $\eta \sim 0.5$, h_{c1} becomes independent of the choice of η. For the range of field $h_{c1} < h < h_{c2}$ a modulated superfluid (LO) phase is realized for any choice of η. h_{c2} is only weakly dependent on the choice of η beyond $\eta \sim 0.5$. For $h > h_{c2}$ the ground state of the system is a partially polarized Fermi liquid (PPFL). In the η-m plane the entire USF regime collapses on to the $m = 0$ axis. The ground state is phase separated (unstable) in this regime and undergoes first-order transition to the LO state beyond a critical polarization m_{c1}, say. A second-order transition from the LO to the PPFL state takes place at m_{c2}. (c) Shows how the polarization (m) varies with the effective field (h) at different mass imbalance ratio η. At the critical effective field h_{c1}, there is a discontinuous transition between the zero and finite polarization states. The transition is only weakly first order at small mass imbalance (as $\eta \to 1$), while a sharp first-order transition is realized in presence of large imbalance in mass.

LO is marked by discontinuity in the polarization, which is shown as the unstable (phase-separated) region in the Fig. 7(b). We observe that the discontinuity in the polarization gets progressively enhanced with increasing imbalance in mass. Irrespective of the system size under consideration, a larger mass imbalance favors a first-order transition between USF and LO phases. A quantitative measure of this discontinuity in polarization can be seen in Fig. 7(c), where we relate the effective field h to the corresponding polarization m.

Although not shown in the figure, the LO regime is segregated into several finer regimes corresponding to the different modulation wave vectors arising at different strength of population imbalance. The optimized wave vector is dictated by the lattice size, interaction strength, as well as the mass imbalance ratio. In the variational scheme that has been used to map out the ground-state phase diagram we have carried out the optimization of energy for different trial solutions corresponding to (i) uniaxial modulation, (ii) diagonal modulation, and (iii) two-dimensional modulations. For the parameter regime under consideration, the uniaxially modulated LO state has been found to be the suitable configuration. In principle, modulations with multiple wave vector make up a possible candidate for the LO state, however, for the sake of numerical simplicity we have not allowed for such solutions in our variational scheme.

The quasiparticle spectra in the LO phase (not shown here) is pseudogapped even at the ground state. The pseudogap behavior in this case is, however, a band structure effect arising out of the underlying modulated state. The corresponding dispersion spectra of this phase deviates significantly from the BCS-type behavior and is characterized by multiple dispersion branches [51]. The multibranched dispersion spectra arise because the electrons now undergo finite-momentum scattering unlike the homogeneous BCS state. The additional van Hove singularities arise from the $\mathbf{k}$ regions where the condition $\partial E_\alpha/\partial \mathbf{k} = 0$ is satisfied by the dispersion spectra, where α correspond to the dispersion branches of the LO spectra [51].

While the choice of the mass imbalance ratio η determines the optimized pairing momenta $\mathbf{Q}$ of the LO superfluid for a particular choice of population imbalance, the coarse features of the spectra (i.e., multiple branches and multiple van Hove singularities) remain unaltered by the choice of η.

2. Finite temperature

The thermal evolution of the system is discussed in terms of m-T phase diagrams shown in Fig. 8 for different choices of mass imbalance ratio η. The thermodynamic phases are determined based on the thermal evolution of pairing field structure factor $S(\mathbf{q})$ and polarization $m(T)$. The broad thermodynamic phases remain the same irrespective of the choice of η, and with increasing imbalance in population the system transits through a breached pair (BP), unstable, LO, and PPFL phases in each case. Also, irrespective of the choice of η there is a tricritical point T_{c1} and a Lifshitz point T_{c2} in the phase diagram. While T_{c1} corresponds to the point where the order of transition changes from second to first within the BP phase, T_{c2} marks the transition from the BP to the LO phase. Unlike the continuum case [35], the two transitions are well separated in a lattice model and the separation increases with increasing mass imbalance. Presence of mass imbalance significantly alters the regime of stability of the different thermodynamic phases. A larger imbalance in mass leads to stronger suppression in T_c and thus a progressively smaller BP regime. The pseudogap regime, on the other hand, increases monotonically with the imbalance in mass, for example, at $h = 0$ the ratio $T^*/T_c \sim 3.33$ at $\eta = 0.2$ and reduces to $\sim$2.14 and $\sim$1.25 at $\eta = 0.4$ and 0.6, respectively.

As discussed in case of the population balanced superfluid, the species-resolved DOS continues to have different thermal disordering scales in the BP regime as well, owing to the different kinetic energy scales of the two species. The underlying superfluid state in this regime is gapped and undergoes thermal evolution to pseudogapped phase with increasing temperature. In Fig. 9 we show the thermal phase diagram of the BP phase

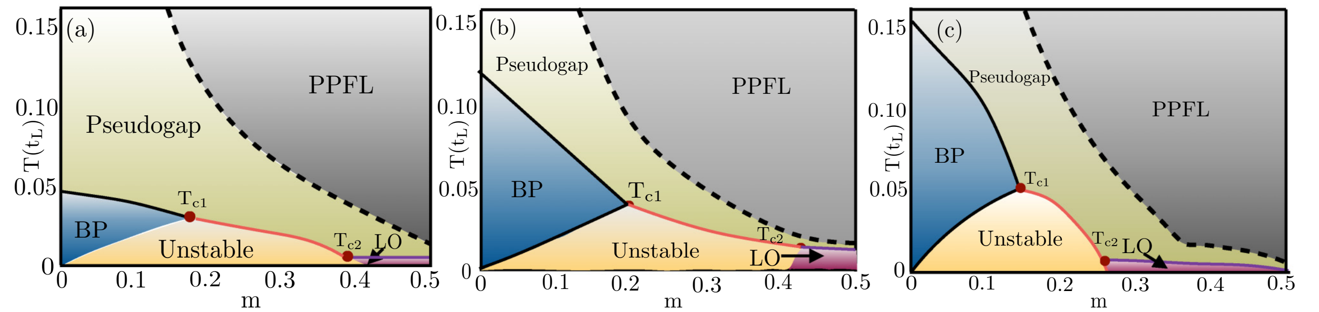

FIG. 8. [$(t_L) \rightarrow$ units of t_L] Polarization-temperature (m-T) phase diagram at selected mass imbalance ratio of $\eta =$ (a) 0.2, (b) 0.4, and (c) 0.6. The dashed line correspond to T^* in each panel. There are three broad thermodynamic phases in each case as the (i) breached pair (BP), (ii) modulated superfluid (LO), and (c) partially polarized Fermi liquid (PPFL). In the regime of weak polarization, the system undergoes second-order thermal transition (shown by black solid line) from BP to the pseudogap phase. At intermediate polarization, the low-temperature phase-separated (unstable) state undergoes a first-order thermal transition (shown by the red solid line). The large polarization regime is LO phase which undergoes a second-order thermal transition. The first-order transition regime is demarcated by a tricritical T_{c1} and a Lifshitz point T_{c2}. A large mass imbalance in the system leads to significant suppression in the T_c and thus the phase coherent superfluid state but gives rise to a wider pseudogap regime.

in the η-T plane for a particular choice of the population imbalance $h = 0.6t_L$. Apart from the T_c there are additional thermal scales in this phase diagram based on the quasiparticle behavior. We discuss them below.

For a population imbalanced system, the species-resolved DOS at the shifted Fermi level ($\omega = \pm h$) shows a nonmonotonic behavior [51]. Increasing temperature leads to progressive filling up of the gap up to a temperature $T_{\max}$. For $T > T_{\max}$, a nonmonotonic thermal evolution sets in and there is now depletion of spectral weight at the Fermi surface with increasing temperature. In presence of strong interaction, the pseudogap continues to survive up to high temperatures but the scale $T_{\max}$ rapidly collapses with increasing population imbalance [51]. Since $T_{\max}$ survives up to temperatures significantly higher than the T_c, it is more likely to be accessible to the experimental probes.

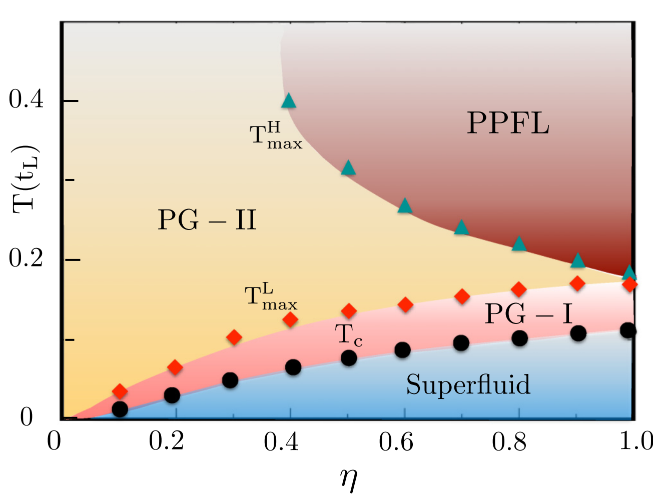

FIG. 9. [$(t_L) \rightarrow$ units of t_L] Mass imbalance-temperature (η-T) phase diagram at fixed population imbalance of $h = 0.6t_L$. Along with the superfluid regime, the figure shows the pseudogap regimes based on the species-resolved DOS. $T^L_{\max}$ and $T^H_{\max}$ correspond to the scales beyond which the pseudogap behavior becomes nonmonotonic (see text). PG-I corresponds to the regime where both the light and heavy species are pseudogapped, while in the PG-II regime only the light species is pseudogapped.

In presence of mass imbalance, the scale $T_{\max}$ is now dependent on the fermion species as $T^H_{\max}$ and $T^L_{\max}$, corresponding to the heavy- and light-fermion species, respectively. $T^L_{\max}$ and $T^H_{\max}$ set the scale for the regime of species-dependent pseudogap behavior. We show these thermal scales in the η-T phase diagram in Fig. 9. There are two pseudogap regions as PG-I and PG-II. While within the PG-I regime both the fermion species are pseudogapped, it is only the light species which is pseudogapped in the PG-II regime. As $\eta \rightarrow 1$, both the scales $T^H_{\max}$ and $T^L_{\max}$ collapse into a single one, as expected from a mass balanced system.

In the LO phase, mass imbalance gives rise to intriguing features both in the thermal and quasiparticle behaviors. For a particular choice of population imbalance, the mass imbalance ratio η dictates the pairing momenta $\mathbf{Q}$. The signature of the same can be observed both in the pairing field structure factor [$S(\mathbf{q})$] as well as in pair correlation $\Gamma(\mathbf{q})$, both of which show peak at $\mathbf{q} \neq 0$. We show the thermal evolution of the same in Fig. 10 at $\eta = 0.6$ and a representative population imbalance of $h = 1.0t_L$, corresponding to the LO phase. At this choice of parameters, the underlying LO phase is uniaxially modulated as can be seen from the twofold symmetry of $S(\mathbf{q})$ and $\Gamma(\mathbf{q})$ at the lowest temperature. With $T_c \sim 0.01t_L$ we find that the state undergoes thermal disordering and acquires a fourfold symmetry $T \approx T_c$. Short-range LO pair correlations, however, continue to survive up to still higher temperatures and vanish only at $T > 2T_c$.

We next show how the finite-momentum pairing in the LO regime modifies the quasiparticle behavior. As mentioned above, the DOS at the shifted Fermi level is pseudogapped even at the ground state and contains additional van Hove singularities. Thermal disordering smears out these singularities. The exact number and location (energy) of the van Hove singularities are altered by the choice of η. We demonstrate this behavior in Fig. 11 where we show the thermal evolution of the species-resolved DOS at two

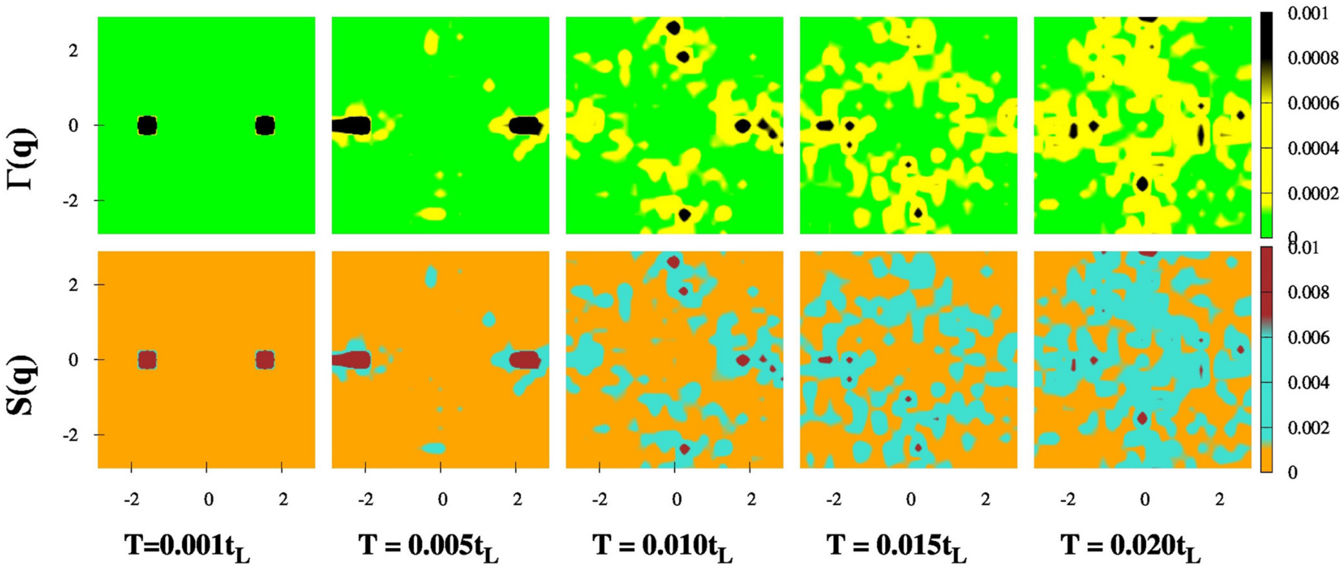

FIG. 10. Thermal evolution of pairing field structure factor [$S(\mathbf{q})$] and pair correlation [$\Gamma(\mathbf{q})$] at a representative point ($h = 1.0t_L$) in the LO phase for a mass imbalance ratio of $\eta = 0.6$ and interaction $U = 4t_L$. The underlying uniaxially modulated LO state is observed through the finite-$\mathbf{Q}$ peaks in $S(\mathbf{q})$ and $\Gamma(\mathbf{q})$, at low temperatures. Fluctuation progressively disorders the system and restores the fourfold symmetry. However, signatures of short-range correlations survive up to $T > 2T_c$ (where $T_c \sim 0.01t_L$). The temperatures are measured in units of t_L.

different η's mentioned in the figure caption. At $\eta = 0.4$ and 0.6, the finite-momentum pairing takes place at $\mathbf{Q} = (0,\pi)$ and $(0,\pi/2)$, respectively. At $T = 0$, the DOS is computed using the variational scheme on a system size of 60×60. We have further compared our ground-state results with the one obtained by Green's function formalism (shown by dotted curve) and have observed qualitative agreement between the two.

Thermal evolution of the species-resolved spectral function $A_\sigma(\mathbf{k},\omega)$ along the $\{0,0\}$ to $\{\pi,\pi\}$ scan across the Brillouin zone for two different choices of η are shown next, in Fig. 12. The multiband nature of the dispersion spectra is evident at low temperatures. In agreement with the DOS, there is no hard gap at the Fermi level, while soft gaps or depletion of spectral weights are observed at the shifted Fermi levels. As in case of the BP phase, the thermal disordering scales continue to be species dependent.

Before closing this section, we discuss about two quantities which crucially depend on the imbalance of population and mass in the system. The first quantity is the momentum-resolved occupation of the fermion species $n_\sigma(\mathbf{k})$, which maps out the Fermi surface architecture. In presence of an underlying inhomogeneous pairing field such as the LO superfluid, we expect a nontrivial Fermi surface and show the same for two different choices of mass imbalance ratio $\eta = 0.4$ and 0.6, in Fig. 13. As in the case of DOS the $T = 0$ calculations are carried out on a larger system size of 60×60 using the variational technique. Apart from the mismatch in size, the Fermi surfaces now show twofold symmetry consequent to the uniaxial modulation of the pairing field at this particular parameter point. Thermal evolution progressively smears out the directional asymmetry in the Fermi surface, and at $T > 2T_c$ the expected fourfold symmetry is restored. Owing to the asymmetry of the Fermi surface, pairing now essentially takes place only at selected $\mathbf{Q}$ values [51].

The second quantity of interest is the low-energy spectral weight distribution $A(\mathbf{k}, 0)$ which gives information about the nature of the superfluid gap. In Fig. 14 we plot $A(\mathbf{k}, 0)$ at $\eta = 0.4$ and 0.6 as it evolves in temperature. A very interesting behavior emerges from this figure, wherein in spite of an isotropic s-wave symmetry of the pairing field, the superfluid gap is now "nodal," arising purely out of the finite-momentum scattering that takes place in the LO phase. The gap isotropy is restored at $T > 2T_c$. Momentum-resolved photoemission spectroscopy is one such experimental tool which can probe the angular dependence of the gap. While the presence of an underlying LO phase guarantees a nodal gap structure, the exact symmetry of the gap (as well as the Fermi surface) is dictated by the pairing momentum $\mathbf{Q}$ and thus by the mass imbalance ratio η. We believe that such nontrivial behavior of the gap would have intriguing signatures in species-resolved transport measurements. We, however, do not touch upon those issues in this paper.

C. Effect of interaction

In the last few sections we have discussed how the interplay of mass and population imbalances bring about several intriguing features in a Fermi-Fermi mixture, at a particular interaction strength. One of the principal advantages of the cold atomic gas quantum emulator is the ability to control the interaction strength and, thus, it is of significant interest to understand how the interplay between the population and mass imbalances alter the well-known picture of BCS-BEC crossover in balanced Fermi gas.

In this section, we briefly discuss the interplay and present our observations in terms of the m-T phase diagram at $\eta = 0.6$ for different choices of interaction strength in Fig. 15. The phase diagram remains qualitatively the same at other mass

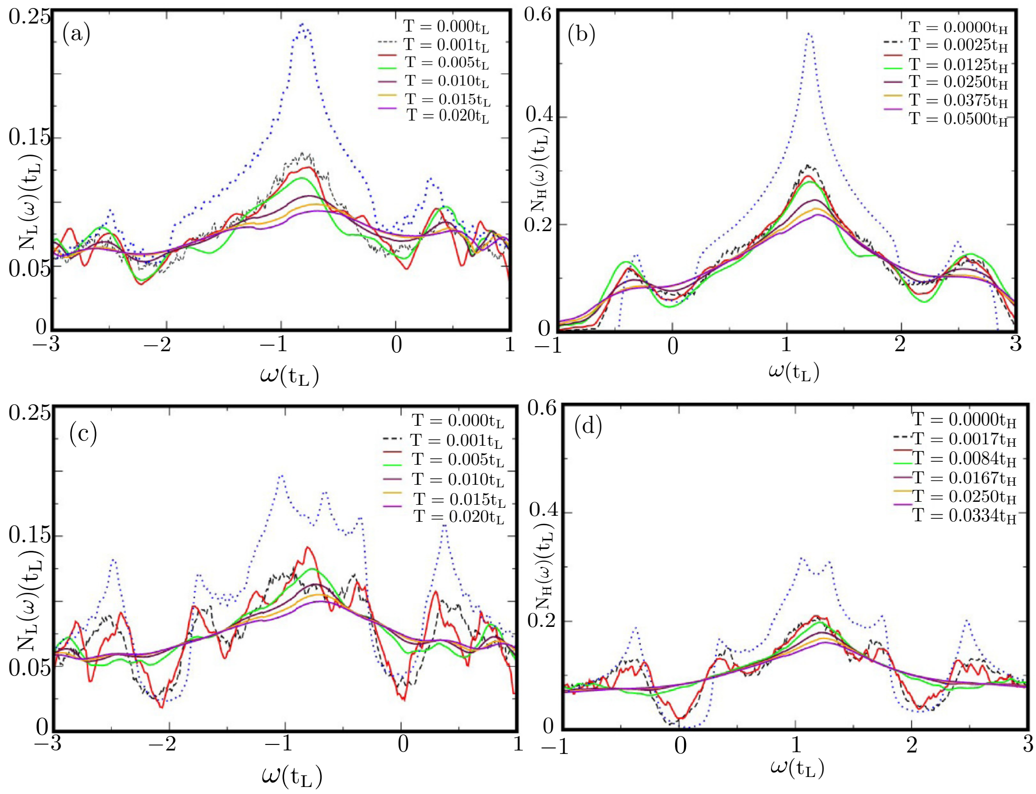

FIG. 11. $[(t_L) \rightarrow$ units of $t_L]$ Thermal evolution of species-resolved DOS at a population imbalance of $h = 1.0t_L$ corresponding to the LO regime, for selected mass imbalance ratio of $\eta = 0.4$ [(a) and (b)] and $\eta = 0.6$ [(c) and (d)]. The state is pseudogapped even at the lowest temperature owing to the band structure effects. Note the additional van Hove singularities that arise due to the underlying modulated state with $\mathbf{Q} = \{0,\pi\}$ at $\eta = 0.4$ and $\mathbf{Q} = \{0,\pi/2\}$ at $\eta = 0.6$. The $T = 0$ DOS is determined from the variational calculation on a lattice size of 60×60, while for $T \neq 0$ we use Monte Carlo simulations on a lattice of size 24×24. The dotted blue curve in each panel corresponds to the results obtained by the Green's function formalism, at the ground state. Access to large system sizes by this technique enables us to demonstrate the van Hove singularities prominently. The results obtained by Green's function formalism agree reasonably with the one obtained through the variational calculations.

imbalance ratio. Figure 15 can roughly be compared with Figs. 8 and 9 of Ref. [35]. In the limit of small polarization, the system is in the breached pair state comprising of uniform superfluidity with finite polarization. Note that we do not make a distinction between a BCS state with a gap at the Fermi level and a Sarma phase with gapless superconductivity, as has been discussed in Ref. [35]. At the interaction regime we are in the BCS description of the state ceases to be valid. At $T \neq 0$ there is spontaneous emergence of islands with nonzero polarization, giving rise to coexisting superfluid and magnetic behavior in the BP phase [51]. At the tricritical point T_{c1} the order of thermal transition changes from second to first *within*

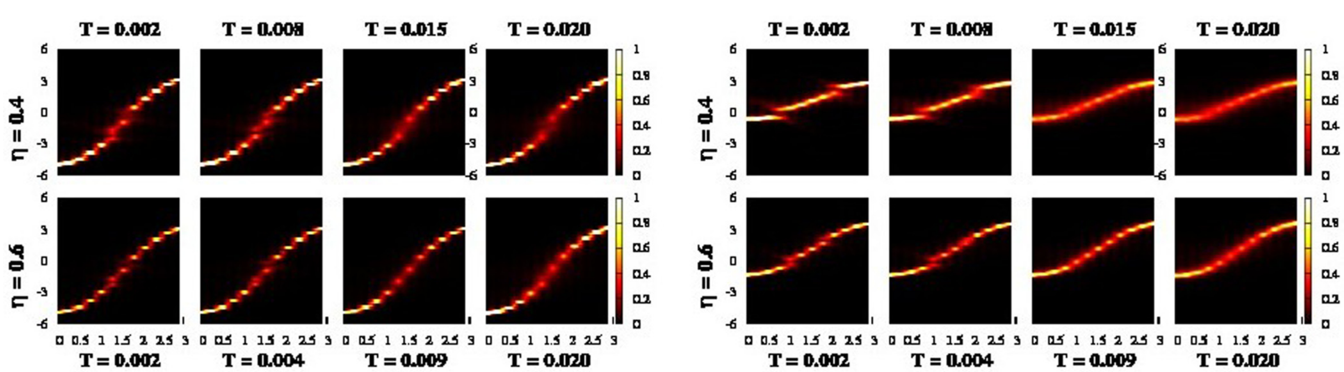

FIG. 12. Thermal evolution of light (left) and heavy (right) species LO spectral function $A(\mathbf{k},\omega)$ across the Brillouin zone for $\mathbf{k} = \{0,0\}$ to $\{\pi,\pi\}$ at $h = 1.0t_L$, $U = 4t_L$ and mass imbalance ratio $\eta = 0.4$ and 0.6. Note the multibranch nature of the dispersion spectra arising due to LO modulations. Note that there is no hard gap at the Fermi level, rather there is depletion of spectral weight at the shifted Fermi level ($\omega = \pm h$). The temperatures are measured in units of t_L.

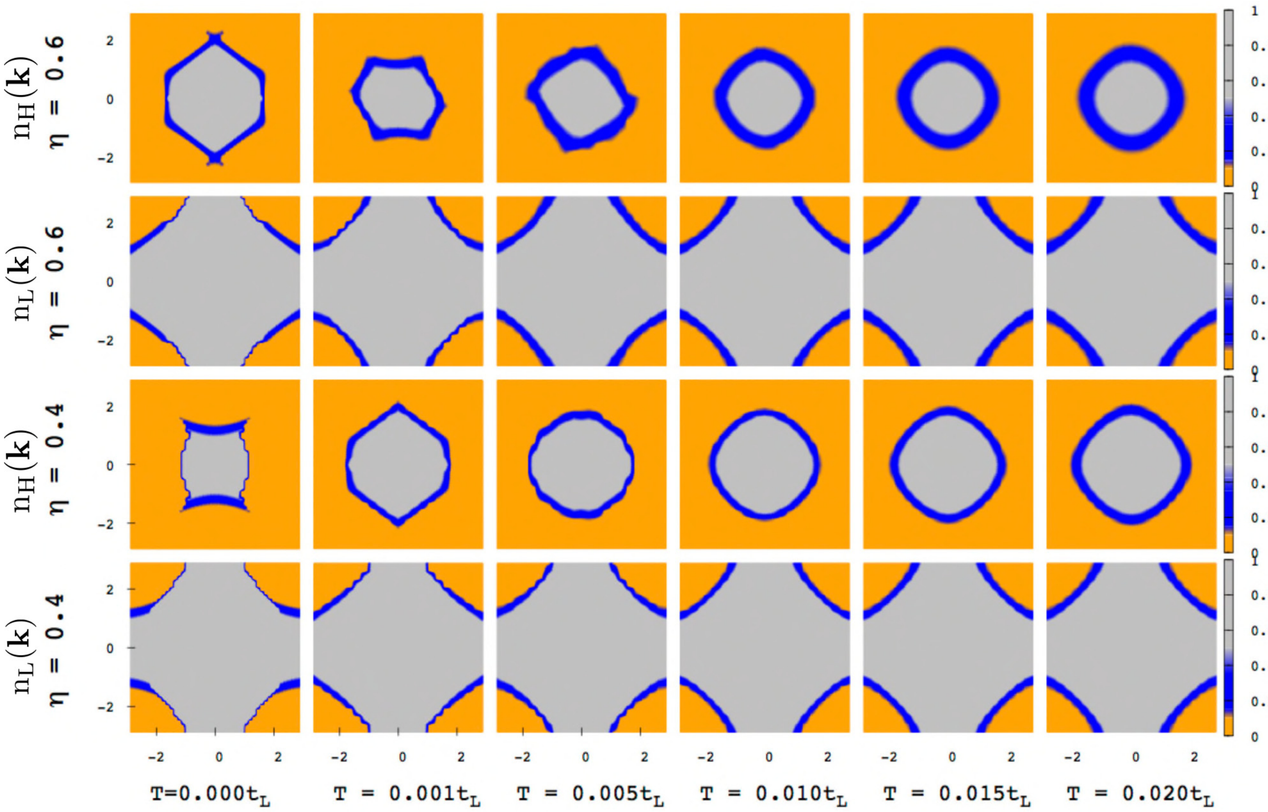

FIG. 13. Thermal evolution of single-particle occupation for the different species $[n_\alpha(\mathbf{k})]$, where $\alpha = L,H$; mapping out the Fermi surface at $\eta = 0.4$ and 0.6 for $h = 1.0t_L$. Note the mismatch in size of the Fermi surfaces owing to the imbalance. The $T = 0$ results are once again obtained using the variational calculation at large system size of $L = 60$. The anisotropy in the Fermi surface architecture arises due to the modulated underlying state. The isotropy of the Fermi surface is regained at high temperature. The temperatures are measured in units of t_L.

the BP phase. Akin to the continuum case [35] the first-order transition is marked by discontinuity in polarization as well as in density. The resulting forbidden region in Figs. 8 and 9 of Ref. [35] is the unstable region in Fig. 15 of this paper. At still larger polarization, a first-order transition takes place between the unstable BP phase and the LO phase at the Lifshitz point T_{c2}. However, it must be noted that in case of lattice fermions for weak and intermediate interactions the T_{c1} and T_{c2} are distinct, unlike the continuum phase diagram where the Lifshitz point coincides with the tricritical point. As shown in Fig. 15, at strong interaction ($U = 6t_L$) there is indeed a single critical point where the BP phase undergoes a second-order

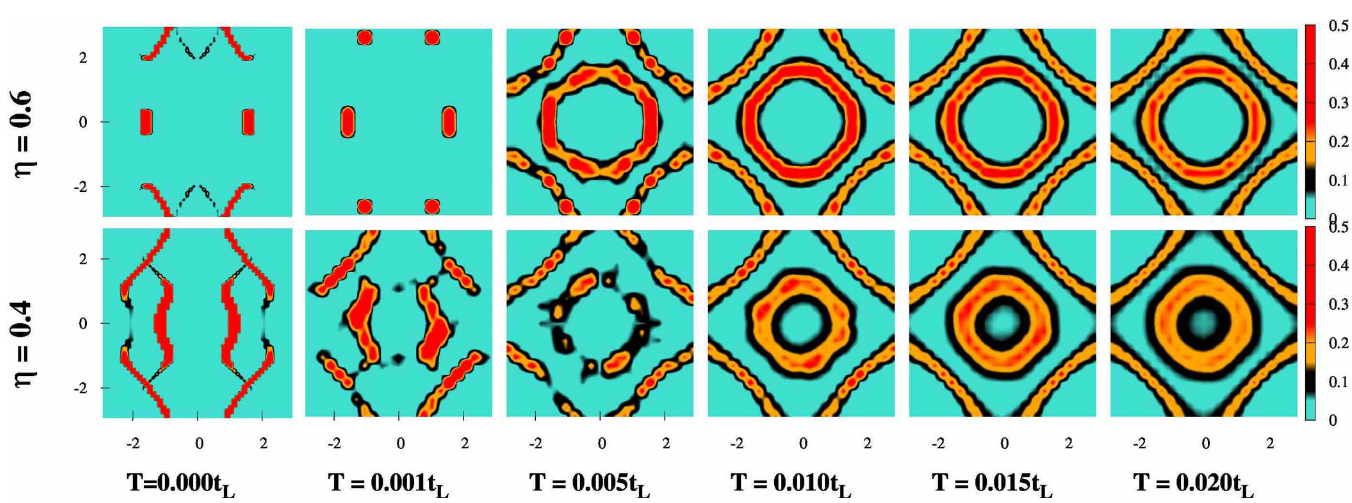

FIG. 14. Thermal evolution of low-energy spectral weight distribution $A(\mathbf{k},0)$ at the Fermi level $\eta = 0.4$ and 0.6, mapping out the superconducting gap structure. Note that in spite of an isotropic s-wave pairing field, a "nodal" gap structure is realized at low temperature. At $T \sim 2T_c$ the gap isotropy is restored. The temperatures are measured in units of t_L.

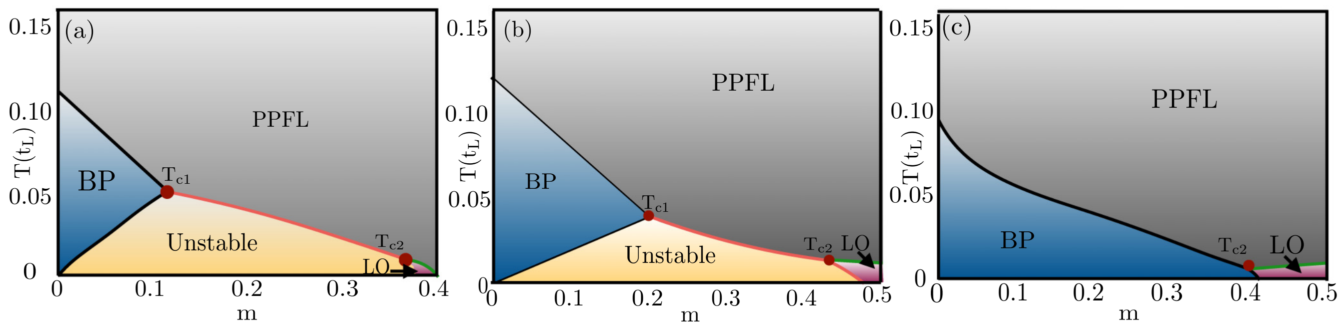

FIG. 15. [$(t_L) \rightarrow$ units of t_L] Polarization-temperature (m-T) phase diagram for $\eta = 0.6$ at different interactions (a) $U = 3t_L$, (b) $U = 4t_L$, and (c) $U = 6t_L$. At strong interaction ($U = 6t_L$) the system undergoes a second-order transition from a BP to LO regime "without" an intervening unstable regime involving first-order transition.

transition to an LO phase, without an intervening first-order unstable regime.

D. Comparison with experiments

We now consider an experimentally realizable Fermi-Fermi mixture and attempt to make some quantitative predictions about it based on our discussions in the previous sections. A suitable candidate for the same is 6_{Li}-40_{K} mixture [18,19,21,22]. Even though superfluidity is yet to be achieved, Feshbach resonance as well as the formation of heteromolecules 6_{Li}-40_{K} has already been attained for this mixture.

In order to analyze the behavior of 6_{Li}-40_{K} mixture, we choose the mass imbalance ratio to be $\eta = 0.15$. For the population imbalance, we select $h = 0.6t_L$ corresponding to the system in BP regime, close to unitarity. We believe that as compared to the LO superfluid regime, the BP phase is more readily accessible to the experimental probes, owing to its higher thermal scales. This justifies our choice of $h = 0.6t_L$.

We begin the discussion of our results by demonstrating the BCS-BEC crossover for the 6_{Li}-40_{K} mixture. Figure 16(a) shows the pairing field structure factor [$S(0,0)$] (at $\mathbf{q} = 0$) across the BCS-BEC crossover. In the intermediate and strong coupling regimes ($U \geqslant 4t_L$) the ground state of the system at this population imbalance corresponds to an unpolarized superfluid (USF). The finite-temperature counterpart of the same leads to the BP phase. In the weak coupling regime ($U < 4t_L$), the system is a partially polarized Fermi liquid (PPFL) in the ground state and does not show any long-range order.

Figure 16(b) shows the temperature dependence of polarization across the BCS-BEC crossover. Increasing interaction suppresses the polarization and uniform superfluid state is realized over a wider regime of temperature. At large interactions where the fermions form tightly bound pairs, the required population imbalance to break the pair and create finite polarization is large, leading to the suppression in the polarization. In striking contrast is the weak ($U < 4t_L$) interaction limit where even at the ground state there is a large finite polarization, indicating a PPFL state.

We present the T_c scale for the 6_{Li}-40_{K} mixture as determined from $S(0, 0)$ in Fig. 16(c). There are two key effects which decide the behavior of the T_c scale. We discuss them pointwise. (i) The primary effect is the suppression of the T_c by the imbalance in mass. Close to unitarity, at $U = 4t_L$ the T_c for a mass balanced system is $T_c^{\mathrm{bal}} \sim 0.15t_L$, in comparison to $T_c^{\mathrm{imb}} \sim 0.03t_L \sim 0.2T_c^{\mathrm{bal}}$ for 6_{Li}-40_{K} mixture. The estimated T_c of the 6_{Li}-40_{K} mixture (at $U = 4t_L$) amounts to $T_c^{\mathrm{imb}} \sim 11.7$ nK. (ii) The second effect on T_c arises out of the population imbalance. A weaker interaction shrinks the regime of both the uniform and modulated superfluid and rapidly gives way to a PPFL state. Thus, at a fixed population imbalance, the system can be in a PPFL state at weak interactions, while a large interaction would correspond to a uniform superfluid state at the same imbalance. Consequently, at a fixed population imbalance, on traversing through the BCS-BEC crossover, a uniform superfluid state would be realized only beyond a critical interaction (U_c). The behavior is significant and is in

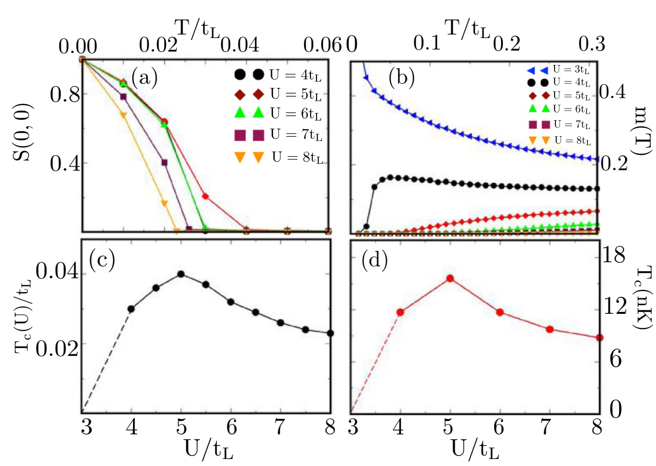

FIG. 16. [$1/t_L \rightarrow$ units of t_L] (a) Pairing field structure factor [$S(0, 0)$] at a population imbalance of $h = 0.6t_L$ and mass imbalance ratio of $\eta = 0.15$ (corresponding to the 6_{Li}-40_{K} mixture) for different interactions. (b) Temperature dependence of polarization [$m(T)$] at different interactions. A large interaction suppresses the polarization. (c) BCS-BEC crossover at $\eta = 0.15$. $T_c(U)$ has its maxima (corresponding to unitarity) at $U = 5t_L$, (d) BCS-BEC crossover replotted in terms of the experimental scales appropriate for the 6_{Li}-40_{K} mixture. Note that at a fixed population imbalance, the uniform superfluidity sets in beyond a critical interaction ($U > U_c$). The dashed line shows that for $U < U_c$, the superfluid order collapses.

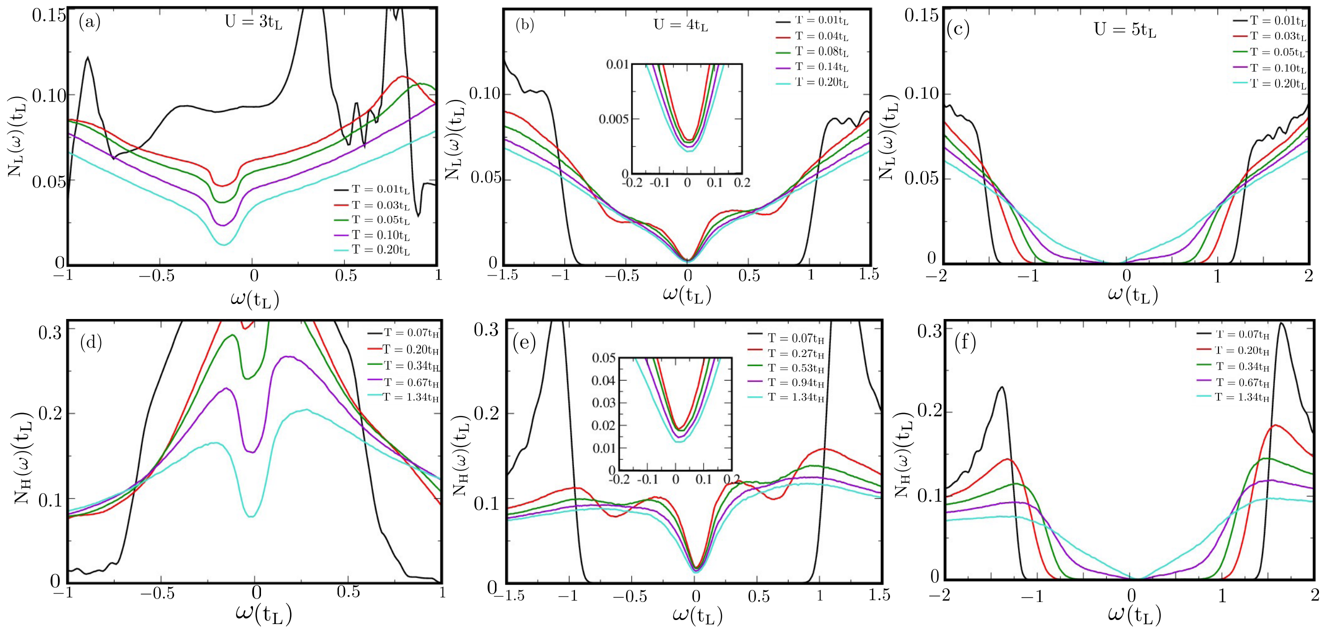

FIG. 17. $[(t_L) \rightarrow$ units of $t_L]$ Density of states (DOS) corresponding to the light- (a)–(c) and heavy-fermion (d)–(f) species for a mass imbalance ratio of $\eta = 0.15$ for selected U-T cross sections. The temperatures corresponding to the two species are normalized by their respective kinetic energy scales. At $U = 3t_L$, in the temperature regime under consideration the DOS pertaining to both species shows nonmonotonic thermal evolution. There is no hard gap at the Fermi level at this interaction since the lowest-temperature state corresponds to a partially polarized Fermi liquid (PPFL). At $U = 4t_L$, the DOS exhibits nonmonotonic behavior with increasing temperature and leads to depletion of the spectral weight at the Fermi level. The onset of nonmonotonicity marks the temperature scales $T^H_{\rm max}$ and $T^L_{\rm max}$ (see text) corresponding to the heavy and light species, respectively. The inset highlights the nonomonotonic behavior close to the Fermi level. At $U = 5t_L$ the thermal evolution of the DOS is monotonic up to a very high temperature, beyond which the scales $T^L_{\rm max}$ and $T^H_{\rm max}$ (not shown in the figure) set in.

contrast to the balanced system in which any arbitrarily small attractive interaction gives rise to a uniform superfluid state.

Figure 16(c) further shows that $T_c(U)$ has a peak at $U = 5t_L$, corresponding to the unitarity in the context of lattice fermion model (see Discussion section). We estimate the $T_c(U)$ scale in experimental units and map out the expected BCS-BEC crossover for the $6_{\rm Li}$-$40_{\rm K}$ mixture in Fig. 16(d). At unitarity, the mixture has a $T_c \sim 15$ nK.

In Fig. 17 we show the thermal evolution of DOS for the two species at different interactions. At $U = 3t_L$ there is no long-range ordered ground state of the system, consequently, there is no hard gap at the Fermi level even at the lowest temperature. There is a depletion in spectral weight at the Fermi level, giving rise to a pseudogap phase. Thermal evolution leads to further depletion of the spectral weight at the Fermi level, in agreement with $m(T)$ [Fig. 16(b)] which shows a reduction in polarization at high temperatures, indicating emergence of short-range correlations. A larger interaction $(4U = t_L)$ gives rise to a hard gap at the Fermi level, which fills up monotonically with temperature before undergoing a nonmonotonic thermal evolution at $T^L_{\rm max}$ $(T^H_{\rm max})$ corresponding to the light (heavy) species. At $U = 5t_L$ the $T^L_{\rm max}$ and $T^H_{\rm max}$ scales are significantly high and are not shown in Fig. 17.

We next analyze the momentum-resolved spectral function A_σ $(\mathbf{k},\omega)$. In Fig. 18 we show the thermal evolution of the species-resolved spectral function at three different interactions, along the $\{0,0\}$ to $\{\pi,\pi\}$ scan across the Brillouin zone. The figure shows species-dependent thermal scales in the problem.

The spectral function for $U = 3t_L$ reveals that at the lowest temperature there is finite weight at the Fermi level and consequently the dispersion spectra are gapless for both the species. Increase in temperature leads to depletion of weight, giving rise to a small but finite gap at the Fermi level. This is a special case of temperature driven gapless to gap transition, arising out of short-range correlations.

We now present the thermal phase diagram across the BCS-BEC crossover for the $6_{\rm Li}$-$40_{\rm K}$ mixture in Fig. 19(a). While in the PG-I regime both $6_{\rm Li}$ and $40_{\rm K}$ would show pseudogap behavior, in the PG-II regime it is only the $6_{\rm Li}$ species which is in the pseudogap phase. $40_{\rm K}$ in the PG-II regime is a partially polarized Fermi liquid. Note that a similar observation has also been made in the context of continuum model [38,57]. Both $T^L_{\rm max}$ and $T^H_{\rm max}$ are significantly higher than T_c and consequently are better accessible to experimental probes, such as rf spectroscopy.

For $6_{\rm Li}$-$40_{\rm K}$ mixture close to unitarity we expect the PG-I regime to survive upto $T^L_{\rm max} \sim 58.5$ nK while the PG-II regime should be observable even at $T^H_{\rm max} \sim 108$ nK, as shown in Fig. 19(b). Another suitable probe is the momentum-resolved spectroscopy which can provide evidence of unequal thermal disordering temperatures corresponding to the two fermion species, a behavior that would be qualitatively similar to the one shown in Fig. 18.

IV. DISCUSSION

The preceding sections comprise the main results of this work. We now touch upon in brief certain aspects on the

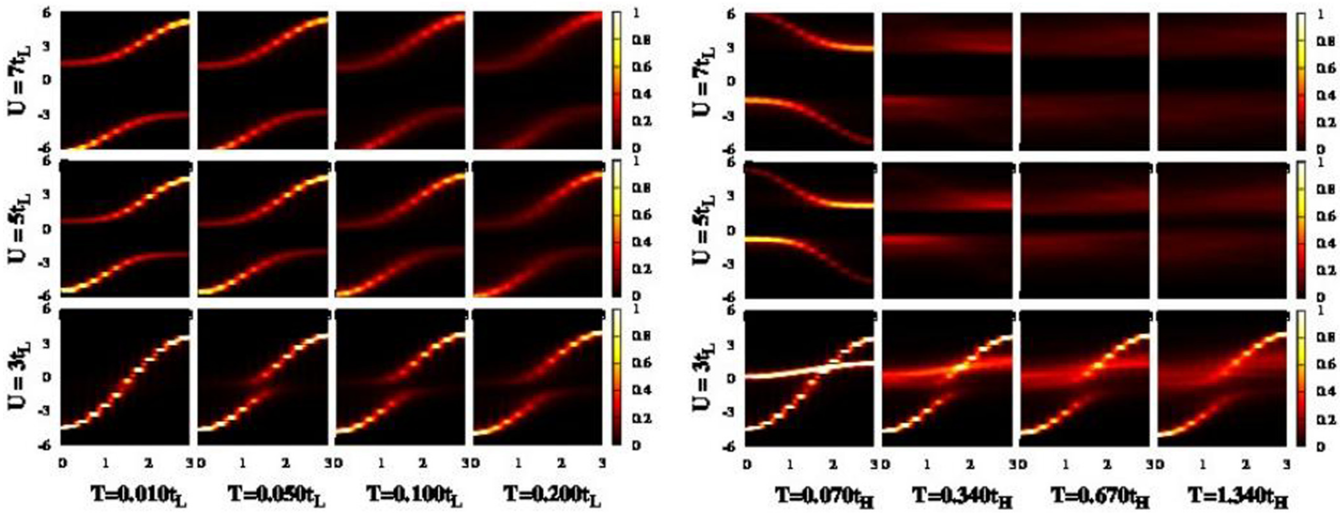

FIG. 18. Spectral function maps along the {0,0} to $\{\pi,\pi\}$ scan across the Brillouin zone for the (left) light- and (right) heavy-fermion species at $\eta = 0.15$ and population imbalance of $h = 0.6t_L$, for different U-T cross sections. Notice that at $U = 3t_L$ increase in temperature opens up a gap at the shifted Fermi level in the dispersion spectra corresponding to both species. The heavy species undergoes faster thermal disordering since it experiences higher scaled temperature.

model under consideration and its connection to cold atomic experiments in continuum; we also discuss about the Green's function formalism that has been used in this work to compute the ground-state quasiparticle properties and benchmark the results obtained with those from Monte Carlo simulations.

A. Connection to continuum unitary gas

The results presented in this paper are based on a lattice fermion model while at the same time they are motivated by experiments on unitary Fermi gas. In this regard, there are few issues that need highlighting. We discuss them below.

1. Concept of unitarity

For the cold atomic gases, the interaction strength is quantified in terms of the s-wave scattering length a_D, with D being the spatial dimensionality. The corresponding coupling constant is defined as $k_F a_D$, where k_F is the Fermi wave vector. For a 3D gas, the limit of unitarity can be defined as the coupling strength at which the first two-body bound state is formed. With $a_{3D} \to \infty$ as $g \to g_c$, where g is the interaction strength, it can be easily seen that $1/k_F a_{3D} = 0$ at g_c, corresponding to unitarity. At the same time, g_c corresponds to the point across the BCS-BEC crossover where the transition temperature is maximum, with $T_c^{\max}/E_F \sim 0.15$ for 3D Fermi gas. Within the framework of a lattice fermion model (3D

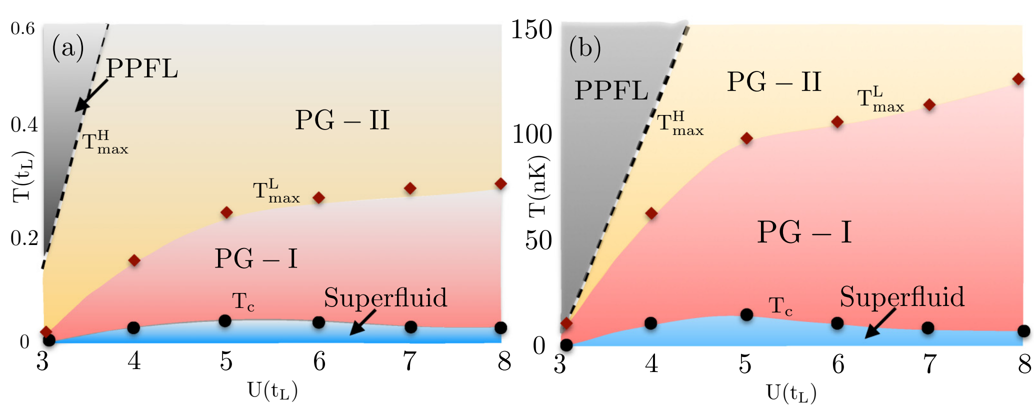

FIG. 19. $[(t_L) \to$ units of $t_L]$ (a) Interaction-temperature (U-T) phase diagram at $\eta = 0.15$ corresponding to the $6_{\rm Li}$-$40_{\rm K}$ mixture. The figure shows the T_c scale along with the pseudogap scales for this mixture at a population imbalance of $h = 0.6t_L$. Both the species exhibit pseudogap behavior in the PG-I regime, while in the PG-II regime only the light species is pseudogapped. The thermal scales of the individual species are defined with respect to their corresponding kinetic energy scales. (b) Thermal scales in terms of the experimental units as would be observable in $6_{\rm Li}$-$40_{\rm K}$ mixture, in species-resolved rf spectroscopy. Close to unitarity ($U = 4t_L$), the pseudogap phase is expected to be observable in both the species up to $T \sim 58$ nK, beyond which the pseudogap feature survives only in the light species up to $T \sim 108$ nK. Thus, even though the $T_c \sim 15$ nk is strongly suppressed in this mixture, short-range pair correlations should be observable up to significantly higher temperatures in experiments.

Hubbard model), it has been found that the first two-body bound state is formed at a critical interaction strength of $U_c/t \sim 7.9$. Interestingly, quantum Monte Carlo (QMC) studies have found that for a 3D system, the maximum T_c is at $U/t \sim 8$ [95]. This brings out the concept that the critical interaction for the formation of two-body bound state in a lattice fermion model coincides with the interaction at maximum T_c.

In case of 2D gas at continuum $a_{2D} \to \infty$ as $g \to 0$, since the two-body bound state is formed at any arbitrary interaction. This definition, however, corresponds to deep inside the BCS regime where a weak coupling description is valid. With increasing interaction the system crosses over to Bose limit as $a_{2D} \to 0$. The coupling at crossover is defined via $\ln(k_F a_{2D}) \to 0$. Interpolation between the BCS and BEC limits showed that maximum T_c occurs at $\ln(k_F a_{2D}) \to 0$, with $T_c^{\max}/E_F \sim 0.1$ [96]. While a 3D-like definition ($a_{2D} \to \infty$ as $g \to 0$) puts the unitarity limit in 2D deep inside the BCS regime, an alternate definition as $[\ln(k_F a_{2D})]^{-1} \to \infty$ is a better choice, first because it captures the crossover between the BCS and BEC regimes correctly and also because it corresponds to the maximum T_c. In other words, the definition $[\ln(k_F a_{2D})]^{-1} \to \infty$ is adequate to capture the two important features of unitarity in 2D, viz., (i) at unitarity neither a pure bosonic nor a fermionic description is sufficient and (ii) the T_c is maximum.

QMC calculation on 2D Hubbard model has shown that the maximum T_c is obtained at $U/t \sim 5$. In our numerical simulations, we call $U/t \sim 4$ being close to unitarity where $T_c \sim 0.9 T_c^{\max}$ [76].

2. *Continuum limit out of lattice model*

The present calculations are carried out at a fixed total chemical potential of $\mu = -0.2t_L$, which is close to the half-filling and the Fermi surface is distinctly noncircular and the lattice effects are dominant. We observe that even in the limit of low density where the Fermi surface is circular and $\epsilon_{\mathbf{k}} \sim k^2$ is a reasonable approximation, it is difficult to capture the continuum effects through the lattice model. At interactions close to unitarity ($U \sim 5t_L$) even if the Fermi levels occupy the lower edge of the band, scattering effects couple the states at upper edge. With these high-energy states being lattice specific, even at low enough densities the results obtained do not match with that of continuum [97,98]. In order to obtain continuum "universal" physics out of lattice simulations, one needs to go to extremely low densities ~0.001, corresponding to lattice size of $\sim 10^4$. This is, however, outside the range of what can be attained in the present day.

B. Single-channel decomposition

In this work, a single-field decomposition in the pairing channel has been used. In general, such a decomposition can not capture the instabilities in all the channels and one needs to take into account the decomposition in the pairing, density, and spin channels, particularly in the FFLO regime. However, in one of our recent works [51] we have shown that even in the FFLO phase the density channel modulations are very weak. Moreover, being away from half-filling, the density modulations are not as important in this study as it would have been at $n = 1$. Decomposition in the additional magnetic channel might lead to quantitative difference in our results. However, while such multichannel decomposition can be readily incorporated within a mean field formalism, a non-Gaussian fluctuation theory like the one presented in this work would be a difficult goal to achieve with a multichannel decomposition. In order to keep the problem numerically tractable, we have chosen for a single-channel decomposition. We believe that inclusion of other channels would not lead to qualitative changes in our results.

C. Effect of quantum fluctuations

One of the principal approximations that has been used in this work is the neglect of the quantum fluctuations. As discussed earlier, we treat the pairing field as classical and retain the spatial fluctuations while neglecting the temporal fluctuations. Within the framework of continuum model, this could be a poor approximation, however, in case of a lattice model it is reasonable. In the continuum FFLO state, the low-energy fluctuation arises from (i) the phase symmetry of the U(1) order parameter, (ii) the translational, and (iii) the rotational symmetry breaking [99]. Consequently, in two-dimensional system, long-range order can not be sustained even at $T = 0$, rendering the corresponding mean field theory invalid. In a lattice model, while the phase field has "XY"-type low-energy excitations, the translational and rotational modes are already gapped out since the spatial symmetry is already broken by the underlying lattice [49]. For example, it is well known that models with XY symmetry show long-range order in 2D and undergo BKT transition at finite temperature. The issue of fluctuation thus reduces to verifying how well the U(1) symmetry T_c is captured by our model in comparison to a full QMC study. A population imbalanced system is difficult to be studied within a QMC approach owing to the fermionic sign problem. However, benchmarking the results for a balanced system as obtained by our technique with those obtained using QMC shows fairly good agreement [100]. The comparison along with the arguments presented above suggests that our technique is suitable to capture the relevant fluctuations and the corresponding finite-temperature behavior.

D. Finite-size effect

We have shown that unlike the balanced system, in presence of population and mass imbalances a critical interaction U_c is required for realizing the uniform ($q = 0$) superfluid state. In order to verify whether the requirement of U_c is an artifact of the finite-size lattice we have carried out the ground state as well as the finite-temperature calculations at different system sizes. Figure 20 shows the mean field ground state at $U = 3t_L$ for different system sizes. We observe that for any system size the superfluid pairing field amplitude is finite up to a population imbalance of $h_c \sim 0.5$. For $h > h_c$ the system is a partially polarized Fermi liquid (PPFL). The figure shows that the regimes of various phases are stable against the choice of the system sizes and one can thus rule out the possibility of the finite-size effect in the results presented in this paper. In order to validate the robustness of our finite-temperature results against the system size effects, we have further calculated (not shown here) the BCS-BEC crossover at various system sizes. We observe no appreciable effect of the system size on the BCS-BEC crossover behavior of the system.

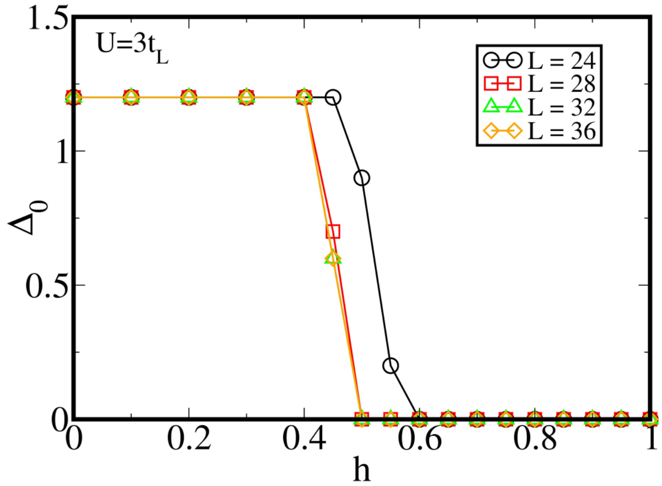

FIG. 20. Variation of the pairing field amplitude with population imbalance at $U = 3t_L$ at the ground state for different system sizes. Notice that for sufficiently large systems, the critical population imbalance marking the phase boundaries is independent of the system size. h is measured in units of t_L.

E. Green's function formalism

The effect of interplay of population and mass imbalance on the quasiparticle properties constitutes one of the key results of this work. It was observed that the single-particle density of states (DOS) deviates significantly from the BCS prediction and reveals additional subgap and supergap features. At the ground state, a low-order approximation of the Green's function of the electron can be set up, which can capture the quasiparticle behavior. The scheme is found to give fairly accurate results over a large $\Delta_0 - \eta - h$ parameter space. The species-resolved Green's function can be approximated as

$$G_{LL}(\mathbf{k},i\omega_n) = \frac{1}{i\omega_n - [\epsilon(\mathbf{k}) + \mu_L] - \Sigma_{LL}(\mathbf{k},i\omega_n)}$$

$$G_{HH}(\mathbf{k},i\omega_n) = \frac{1}{i\omega_n - [\epsilon(\mathbf{k}) + \mu_H] - \Sigma_{HH}(\mathbf{k},i\omega_n)},$$

where

$$\Sigma_{LL}(\mathbf{k},i\omega_n) = \frac{|\Delta_0|^2}{4}\left\{\frac{1}{[\omega + \epsilon(-\mathbf{k} - \mathbf{Q}) - \mu_H]} + \frac{1}{[\omega + \epsilon(-\mathbf{k} + \mathbf{Q}) - \mu_H]}\right\},$$

$$\Sigma_{HH}(\mathbf{k},i\omega_n) = \frac{|\Delta_0|^2}{4}\left\{\frac{1}{[\omega + \epsilon(-\mathbf{k} - \mathbf{Q}) - \mu_L]} + \frac{1}{[\omega + \epsilon(-\mathbf{k} + \mathbf{Q}) - \mu_L]}\right\}$$

with $\epsilon_{ii}(\mathbf{k}) = -2t_{ii}[\cos(k_x + \cos(k_y)]$ where, $ii = L,H$. From the above expressions one can extract the spectral function as

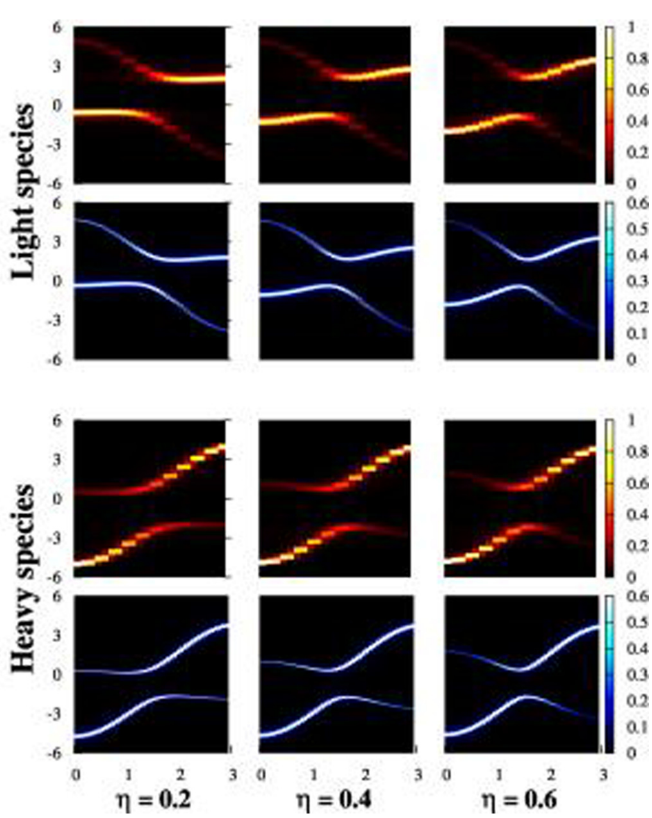

FIG. 21. Dispersion spectrum of the two species in the BP regime ($h = 0.6t_L$) obtained through the BdG calculation (top panels) in comparison to those obtained through Green's function formalism (bottom panels) at different mass imbalance ratio η.

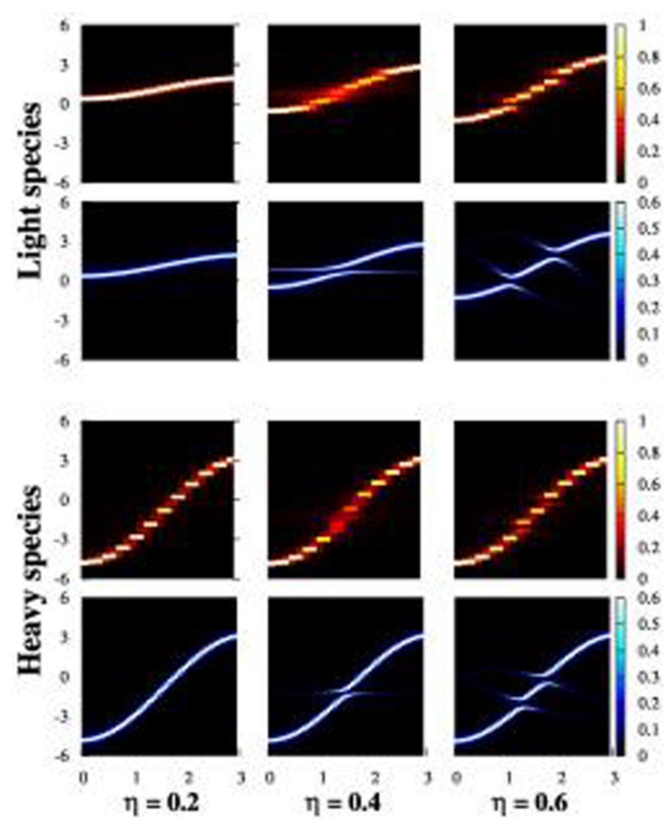

FIG. 22. Dispersion spectrum of the two species in the LO regime ($h = t_L$) obtained through the BdG calculation (top panels) in comparison to those obtained through Green's function formalism (bottom panels) at different mass imbalance ratio η.

$A_{LL}(\mathbf{k},\omega) = -(1/\pi)\mathrm{Im}G_{LL}(\mathbf{k},\omega + i\delta)\,|_{\delta\to 0}$. Similar expression can be obtained for $A_{HH}(\mathbf{k},\omega)$.

In Figs. 21 and 22 we have compared our results obtained through Monte Carlo simulations with those obtained through the Green's function formalism at $h = 0.6t_L$ and $1.0t_L$, representative of the BP and LO phases, respectively. We have shown the spectral function $[A_\sigma(\mathbf{k},\omega)]$ maps at different mass imbalance ratio η for the light- and heavy-fermion species. The agreement between the results obtained through the two techniques is fairly good, and along with capturing the species-dependent behavior of the dispersion spectra, the technique also reproduces the multibranched dispersion spectra for the LO state. The agreement justifies our choice of the Green's function formalism to access quasiparticle behavior at large system sizes at the ground state.

V. CONCLUSIONS

In conclusion, we have investigated the BCS-BEC crossover of mass imbalanced Fermi-Fermi mixture within the framework of a two-dimensional lattice fermion model. We have mapped out the thermal phase diagram in the η-T plane and have shown how the thermal scales are suppressed by the imbalance in mass. Further, investigation of the quasiparticle behavior revealed that unlike the balanced superfluid, the Fermi-Fermi mixture comprises of two pseudogap regimes as PG-I, in which the single-particle excitation spectra of both the species are pseudogapped and PG-II, where only the light species is pseudogapped. We have further investigated the interplay of population imbalance in such Fermi-Fermi mixtures and have shown that at a fixed imbalance in population uniform superfluidity is realized only beyond a critical U_c unlike the balanced superfluid. Moreover, it was shown that a modulated LO superfluid state gives rise to a nodal superfluid gap in spite of an s-wave pairing field symmetry. We have made quantitative predictions of the thermal scales pertaining to the 6_{Li}-40_{K} mixture and have suggested that experimental techniques such as rf and momentum-resolved photoemission spectroscopy can be used to probe the PG-I regime upto $T \sim 58$ nK and PG-II regime up to $T > 108$ nK, in this mixture, close to the unitarity. While the T_c is strongly suppressed in this mixture, signatures of short-range pair correlation survive up to significantly higher temperatures. We believe that our results can serve as suitable benchmarks for the experimental observations of 6_{Li}-40_{K} mixture.

ACKNOWLEDGMENTS

The author gratefully acknowledges Professor P. Majumdar for the insightful comments on the manuscript. The HPC cluster facility of Harish Chandra Research Institute, Allahabad, is duly acknowledged. A part of this work was carried out at IMSc, Chennai, India, and the author acknowledges the hospitality provided during the visit.

[1] C. A. Regal, M. Greiner, and D. S. Jin, Phys. Rev. Lett. **92**, 040403 (2004).
[2] M. W. Zwierlein, C. A. Stan, C. H. Schunck, S. M. F. Raupach, A. J. Kerman, and W. Ketterle, Phys. Rev. Lett. **92**, 120403 (2004).
[3] J. Kinast, S. L. Hemmer, M. E. Gehm, A. Turlapov, and J. E. Thomas, Phys. Rev. Lett. **92**, 150402 (2004).
[4] M. Bartenstein, A. Altmeyer, S. Riedl, S. Jochim, C. Chin, J. H. Denschlag, and R. Grimm, Phys. Rev. Lett. **92**, 203201 (2004).
[5] C. A. Regal, C. Ticknor, J. L. Bohn, and D. S. Jin, Phys. Rev. Lett. **90**, 053201 (2003).
[6] J. Zhang, E. G. M. van Kempen, T. Bourdel, L. Khaykovich, J. Cubizolles, F. Chevy, M. Teichmann, L. Tarruell, S. J. J. M. F. Kokkelmans, and C. Salomon, Phys. Rev. A **70**, 030702 (2004).
[7] C. H. Schunck, M. W. Zwierlein, C. A. Stan, S. M. F. Raupach, W. Ketterle, A. Simoni, E. Tiesinga, C. J. Williams, and P. S. Julienne, Phys. Rev. A **71**, 045601 (2005).
[8] Y. Ohashi, Phys. Rev. Lett. **94**, 050403 (2005).
[9] T.-L. Ho and R. B. Diener, Phys. Rev. Lett. **94**, 090402 (2005).
[10] V. Gurarie, L. Radzihovsky, and A. V. Andreev, Phys. Rev. Lett. **94**, 230403 (2005).
[11] J. Levinsen, N. R. Cooper, and V. Gurarie, Phys. Rev. Lett. **99**, 210402 (2007).
[12] M. Iskin and C. A. R. Sá de Melo, Phys. Rev. B **72**, 224513 (2005).
[13] D. Inotani, R. Watanabe, M. Sigrist, and Y. Ohashi, Phys. Rev. A **85**, 053628 (2012).
[14] G. Sarma, J. Phys. Chem. Solids **24**, 1029 (1963).
[15] W. V. Liu and F. Wilczek, Phys. Rev. Lett. **90**, 047002 (2003).
[16] M. M. Forbes, E. Gubankova, W. V. Liu, and F. Wilczek, Phys. Rev. Lett. **94**, 017001 (2005).
[17] D. E. Sheehy and L. Radzihovsky, Ann. Phys. **322**, 1790 (2007).
[18] E. Wille, F. M. Spiegelhalder, G. Kerner, D. Naik, A. Trenkwalder, G. Hendl, F. Schreck, R. Grimm, T. G. Tiecke, J. T. M. Walraven, S. J. J. M. F. Kokkelmans, E. Tiesinga, and P. S. Julienne, Phys. Rev. Lett. **100**, 053201 (2008).
[19] M. Taglieber, A.-C. Voigt, T. Aoki, T. W. Hänsch, and K. Dieckmann, Phys. Rev. Lett. **100**, 010401 (2008).
[20] A.-C. Voigt, M. Taglieber, L. Costa, T. Aoki, W. Wieser, T. W. Hänsch, and K. Dieckmann, Phys. Rev. Lett. **102**, 020405 (2009).
[21] L. Costa, J. Brachmann, A.-C. Voigt, C. Hahn, M. Taglieber, T. W. Hänsch, and K. Dieckmann, Phys. Rev. Lett. **105**, 269903(E) (2010).
[22] D. Naik, A. Trenkwalder, C. Kohstall, F. M. Spiegelhalder, M. Zaccanti, G. Hendl, F. Schreck, R. Grimm, T. M. Hanna, and P. S. Julienne, Eur. Phys. J. D **65**, 55 (2011).
[23] F. M. Spiegelhalder, A. Trenkwalder, D. Naik, G. Kerner, E. Wille, G. Hendl, F. Schreck, and R. Grimm, Phys. Rev. A **81**, 043637 (2010).
[24] T. G. Tiecke, M. R. Goosen, A. Ludewig, S. D. Gensemer, S. Kraft, S. J. J. M. F. Kokkelmans, and J. T. M. Walraven, Phys. Rev. Lett. **104**, 053202 (2010).
[25] G.-D. Lin, W. Yi, and L.-M. Duan, Phys. Rev. A **74**, 031604 (2006).
[26] S.-T. Wu, C.-H. Pao, and S.-K. Yip, Phys. Rev. B **74**, 224504 (2006).

[27] M. Iskin and C. A. R. Sá de Melo, Phys. Rev. Lett. **97**, 100404 (2006).
[28] M. Iskin and C. A. R. Sá de Melo, Phys. Rev. A **76**, 013601 (2007).
[29] C.-H. Pao, S.-T. Wu, and S.-K. Yip, Phys. Rev. A **76**, 053621 (2007).
[30] M. M. Parish, F. M. Marchetti, A. Lamacraft, and B. D. Simons, Phys. Rev. Lett. **98**, 160402 (2007).
[31] G. Orso, L. P. Pitaevskii, and S. Stringari, Phys. Rev. A **77**, 033611 (2008).
[32] A. Gezerlis, S. Gandolfi, K. E. Schmidt, and J. Carlson, Phys. Rev. Lett. **103**, 060403 (2009).
[33] R. B. Diener and M. Randeria, Phys. Rev. A **81**, 033608 (2010).
[34] N. Takemori and A. Koga, J. Phys. Soc. Jpn. **81**, 063002 (2012).
[35] J. E. Baarsma, K. B. Gubbels, and H. T. C. Stoof, Phys. Rev. A **82**, 013624 (2010).
[36] J. E. Baarsma, J. Armaitis, R. A. Duine, and H. T. C. Stoof, Phys. Rev. A **85**, 033631 (2012).
[37] Z. Lan, G. M. Bruun, and C. Lobo, Phys. Rev. Lett. **111**, 145301 (2013).
[38] R. Hanai, T. Kashimura, R. Watanabe, D. Inotani, and Y. Ohashi, Phys. Rev. A **88**, 053621 (2013).
[39] Y.-J. Lin, K. Jimenez-Garcia, and I. B. Spielman, Nature (London) **471**, 83 (2011).
[40] P. Wang, Z.-Q. Yu, Z. Fu, J. Miao, L. Huang, S. Chai, H. Zhai, and J. Zhang, Phys. Rev. Lett. **109**, 095301 (2012).
[41] L. W. Cheuk, A. T. Sommer, Z. Hadzibabic, T. Yefsah, W. S. Bakr, and M. W. Zwierlein, Phys. Rev. Lett. **109**, 095302 (2012).
[42] L. Jiang, X.-J. Liu, H. Hu, and H. Pu, Phys. Rev. A **84**, 063618 (2011).
[43] G. B. Partridge, W. Li, Y. A. Liao, R. G. Hulet, M. Haque, and H. T. C. Stoof, Phys. Rev. Lett. **97**, 190407 (2006).
[44] Y.-i. Shin, C. H. Schunck, A. Schirotzek, and W. Ketterle, Nature (London) **451**, 689 (2008).
[45] C. H. Schunck, Y. Shin, A. Schirotzek, M. W. Zwierlein, and W. Ketterle, Science **316**, 867 (2007).
[46] Y. Shin, M. W. Zwierlein, C. H. Schunck, A. Schirotzek, and W. Ketterle, Phys. Rev. Lett. **97**, 030401 (2006).
[47] Y.-a. Liao, A. S. C. Rittner, T. Paprotta, W. Li, G. B. Partridge, R. G. Hulet, S. K. Baur, and E. J. Mueller, Nature (London) **467**, 567 (2010).
[48] T. K. Koponen, T. Paananen, J.-P. Martikainen, and P. Törmä, Phys. Rev. Lett. **99**, 120403 (2007).
[49] Y. L. Loh and N. Trivedi, Phys. Rev. Lett. **104**, 165302 (2010).
[50] M. J. Wolak, B. Grémaud, R. T. Scalettar, and G. G. Batrouni, Phys. Rev. A **86**, 023630 (2012).
[51] M. Karmakar and P. Majumdar, Phys. Rev. A **93**, 053609 (2016).
[52] M. Karmakar and P. Majumdar, Eur. Phys. J. D **70**, 220 (2016).
[53] L. He, M. Jin, and P. Zhuang, Phys. Rev. B **73**, 214527 (2006).
[54] L. He, M. Jin, and P. Zhuang, Phys. Rev. B **74**, 214516 (2006).
[55] D. Roscher, J. Braun, and J. E. Drut, Phys. Rev. A **91**, 053611 (2015).
[56] J. Braun, J. E. Drut, T. Jahn, M. Pospiech, and D. Roscher, Phys. Rev. A **89**, 053613 (2014).
[57] R. Hanai and Y. Ohashi, Phys. Rev. A **90**, 043622 (2014).
[58] H. Guo, C.-C. Chien, Q. Chen, Y. He, and K. Levin, Phys. Rev. A **80**, 011601 (2009).
[59] G. G. Batrouni, M. J. Wolak, F. Hbert, and V. G. Rousseau, Europhys. Lett. **86**, 47006 (2009).
[60] M. Lu, N. Q. Burdick, and B. L. Lev, Phys. Rev. Lett. **108**, 215301 (2012).
[61] A. Frisch, K. Aikawa, M. Mark, F. Ferlaino, E. Berseneva, and S. Kotochigova, Phys. Rev. A **88**, 032508 (2013).
[62] P. Pieri, A. Perali, G. C. Strinati, S. Riedl, M. J. Wright, A. Altmeyer, C. Kohstall, E. R. Sánchez Guajardo, J. Hecker Denschlag, and R. Grimm, Phys. Rev. A **84**, 011608 (2011).
[63] S. Nascimbne, N. Navon, K. J. Jiang, F. Chevy, and C. Salomon, Nature (London) **463**, 1057 (2010).
[64] K. B. Gubbels, J. E. Baarsma, and H. T. C. Stoof, Phys. Rev. Lett. **103**, 195301 (2009).
[65] M. O. J. Heikkinen, D.-H. Kim, and P. Törmä, Phys. Rev. B **87**, 224513 (2013).
[66] M. O. J. Heikkinen, D.-H. Kim, M. Troyer, and P. Törmä, Phys. Rev. Lett. **113**, 185301 (2014).
[67] S. Chiesa and S. Zhang, Phys. Rev. A **88**, 043624 (2013).
[68] J. Braun, J. E. Drut, and D. Roscher, Phys. Rev. Lett. **114**, 050404 (2015).
[69] C. A. R. Sá de Melo, M. Randeria, and J. R. Engelbrecht, Phys. Rev. Lett. **71**, 3202 (1993).
[70] R. Haussmann, W. Rantner, S. Cerrito, and W. Zwerger, Phys. Rev. A **75**, 023610 (2007).
[71] A. Perali, P. Pieri, L. Pisani, and G. C. Strinati, Phys. Rev. Lett. **92**, 220404 (2004).
[72] E. Burovski, N. Prokof'ev, B. Svistunov, and M. Troyer, Phys. Rev. Lett. **96**, 160402 (2006).
[73] A. Bulgac, J. E. Drut, and P. Magierski, Phys. Rev. Lett. **99**, 120401 (2007).
[74] V. K. Akkineni, D. M. Ceperley, and N. Trivedi, Phys. Rev. B **76**, 165116 (2007).
[75] M. Randeria and E. Taylor, Annu. Rev. Condens. Matter Phys. **5**, 209 (2014).
[76] T. Paiva, R. Scalettar, M. Randeria, and N. Trivedi, Phys. Rev. Lett. **104**, 066406 (2010).
[77] W. E. Evenson, J. R. Schrieffer, and S. Q. Wang, J. Appl. Phys. **41**, 1199 (1970).
[78] Y. Dubi, Y. Meir, and Y. Avishai, Nature (London) **449**, 876 (2007).
[79] P. Nozières and S. Schmitt-Rink, J. Low Temp. Phys. **59**, 195 (1985).
[80] H. Tamaki, Y. Ohashi, and K. Miyake, Phys. Rev. A **77**, 063616 (2008).
[81] N. Dupuis, Phys. Rev. B **70**, 134502 (2004).
[82] T. K. Kopeć, Phys. Rev. B **65**, 054509 (2002).
[83] R. T. Scalettar, E. Y. Loh, J. E. Gubernatis, A. Moreo, S. R. White, D. J. Scalapino, R. L. Sugar, and E. Dagotto, Phys. Rev. Lett. **62**, 1407 (1989).
[84] N. Trivedi and M. Randeria, Phys. Rev. Lett. **75**, 312 (1995).
[85] S. Allen, H. Touchette, S. Moukouri, Y. M. Vilk, and A.-M. S. Tremblay, Phys. Rev. Lett. **83**, 4128 (1999).
[86] M. Keller, W. Metzner, and U. Schollwöck, Phys. Rev. Lett. **86**, 4612 (2001).
[87] M. Capone, C. Castellani, and M. Grilli, Phys. Rev. Lett. **88**, 126403 (2002).
[88] A. Toschi, M. Capone, and C. Castellani, Phys. Rev. B **72**, 235118 (2005).
[89] A. Toschi, P. Barone, M. Capone, and C. Castellani, New J. Phys. **7**, 7 (2005).

[90] A. Garg, H. R. Krishnamurthy, and M. Randeria, Phys. Rev. B **72**, 024517 (2005).
[91] S. Kumar and P. Majumdar, Eur. Phys. J. B **50**, 571 (2006).
[92] J. P. Gaebler, J. T. Stewart, T. E. Drake, D. S. Jin, A. Perali, P. Pieri, and G. C. Strinati, Nat. Phys. **6**, 569 (2010).
[93] P. Fulde and R. A. Ferrell, Phys. Rev. **135**, A550 (1964).
[94] A. I. Larkin and Y. N. Ovchinnikov, Zh. Eksp. Teor. Fiz. **47**, 1136 (1964) [Sov. Phys. JETP **20**, 762 (1965)].
[95] A. Sewer, X. Zotos, and H. Beck, Phys. Rev. B **66**, 140504 (2002).
[96] M. G. Ries, A. N. Wenz, G. Zürn, L. Bayha, I. Boettcher, D. Kedar, P. A. Murthy, M. Neidig, T. Lompe, and S. Jochim, Phys. Rev. Lett. **114**, 230401 (2015).
[97] A. Privitera, M. Capone, and C. Castellani, Phys. Rev. B **81**, 014523 (2010).
[98] A. Privitera and M. Capone, Phys. Rev. A **85**, 013640 (2012).
[99] L. Radzihovsky, Phys. Rev. A **84**, 023611 (2011).
[100] S. Tarat and P. Majumdar, Europhys. Lett. **105**, 67002 (2014).